Petroleum Science 18 (2021) 1240–1255

Contents lists available at ScienceDirect

Petroleum Science

journal homepage: www.keaipublishing.com/en/journals/petroleum-science

Original Article

The dispersion of particles in turbulent semi-circular duct flows

Min Liu [a, b], Jun Yao [a, b], Yan-Lin Zhao [a, b, *]

[a] International Joint Laboratory on Clean Energy Science and Technology, College of Mechanical and Transportation Engineering, China University of Petroleum-Beijing, Beijing, 102249, People's Republic of China
[b] Beijing Key Laboratory of Process Fluid Filtration and Separation, College of Mechanical and Transportation Engineering, China University of Petroleum-Beijing, Beijing, 102249, People's Republic of China

ARTICLE INFO

Article history:
Received 14 September 2020
Accepted 29 March 2021
Available online 24 May 2021

Edited by: Xiu-Qiu Peng and Teng Zhu

Keywords:
Semi-circular duct
Secondary flow
Particle dispersion
Turbulence
Large eddy simulation

ABSTRACT

The flow field in a semi-circular duct is simulated by Large Eddy Simulation (LES) and its particle field is simulated by Lagrange particle tracking method. Reynolds number Re_b (based on bulk velocity and hydraulic diameter) is 80,000 and Re_τ (based on friction velocity and hydraulic diameter) is 3528. Particle diameter d_p is chosen as 10, 50, 100, 500 μm corresponding to St as 0.10, 2.43, 9.72, 243.05. The results show that the intensity of the secondary flow near the ceiling is less than that near the floor because the ceiling is curved and able to inhibit the secondary flow. It is found that the difference between the semi-circular duct and the square duct is that the secondary flow in a corner of the semi-circular duct is not symmetrical along the diagonal although they have the same generation mechanism. Regarding the particles, small particles ($d_p \leq 10$ μm) are found to uniformly distribute in the duct, while large particles ($d_p \geq 50$ μm) preferentially distribute in the corner and floor center. The maximum particles ($d_p = 500$ μm) fall on the floor quickly and their dispersion mainly depends on the secondary flow near the floor. Particle deposition in the corner depends on particle size due to the effect of secondary flow and gravity. The effect of lift force on particles becomes more significant for 50 and 100 μm particles in comparison with other smaller particles. In the end, the effect of secondary flow is found to be more significant to dominate particle behavior than that of flow fluctuation.

1. Introduction

Ducts are widely used in computer components, equipment connections, reaction rooms, separators and so on. Regarding the geometry of the duct cross sections, circle and square are most found while hexagon, trapezoid and semi-circle could be also found. Based on the application of semi-circular duct in the entrance of rotary kiln, Larsson et al. (2011) conducted experiment and numerical simulation on the flow field in the semi-circular duct and obtained the characteristics of the flow field. Semi-circular ducts could be found in industries and daily life. For example, in granular pneumatic conveying systems, granules like to deposit at the duct bottom gradually and cause the circular duct to become a semi-circular duct. In addition, in recent years, the building drainage pipe began to replace the circular duct by the semi-circular duct in order to meet with the requirement by local situation. In industry, the impurities in the desulfurization pipelines, the particles in the flue gas purification pipelines of power plants, the hydrates in the oil pipelines and the erosion-corrosion products in the chemical pipelines all tend to cause the circular pipe to become a semi-circular duct. However, the investigation of the flow in a semi-circular duct is little and the multiphase flow in it has never been found. This is the original motive to do this work including the characterizes of single phase flow in a semi-circular duct as well as particle behavior (dispersion and deposition) in it.

Secondary flow is the principle characterize of the semi-circular duct flow. It is known that the secondary flow can be divided into Prandtl's first and second kind secondary flow upon two different working mechanisms (Bradshaw, 1987). The first is due to pressure-driven, for example the secondary flow can be found in a bend and its velocity is about 30% of the bulk velocity (Liou et al., 2003; Shimizu et al., 1992; Westra et al., 2010). The second is due to turbulence driven and found in noncircular ducts, such as the square duct (with 1–2% of the bulk velocity) and the semi-circular

* Corresponding author. International Joint Laboratory on Clean Energy Science and Technology, College of Mechanical and Transportation Engineering, China University of Petroleum-Beijing, Beijing, 102249, People's Republic of China.
E-mail address: ylzhao@cup.edu.cn (Y.-L. Zhao).

https://doi.org/10.1016/j.petsci.2021.05.004

duct (Pirozzoli et al., 2018).

The secondary flow occurred in a square duct is first found and confirmed by Nikuradse (1930). Since then, more and more experimental works have been developed to improve the theory. With the progress of computer technology, numerical simulations were used to investigate the secondary flow (Brundrett and Baines, 1964; Gessner and Jones, 1965). The simulation of turbulence in a square duct by Reynolds stresses model (Launder and Ying, 1972) indicated that the secondary flow is related to the anisotropy of Reynolds stresses while isotropic turbulence model was unable to present the secondary flow. Moreover, it is confirmed that the secondary flow does not occur in a laminar flow (Madabhushi and Vanka, 1991). In recent years, some advanced computation technologies have been developed to study the secondary flow in square duct flows including LES (Breuer and Rodi, 1994) and DNS (Gavrilakis, 1992).

The secondary flow in a square duct is composed of two symmetrical eddies at each corner. For each eddy, the fluid flows diagonally from the duct center to the duct corner, and then move along the floor from the corner to the floor centre. The magnitude of the secondary flow velocity is about 1–2% of that of the streamwise flow. Due to being perpendicular to each other, the secondary flow plays a significant role at the cross section and causes the contour of streamwise mean velocity to bulge towards the corner (Gavrilakis, 1992). The working mechanism of the secondary flow was discovered by DNS (Huser and Biringen, 1993) for a square duct. It is found that the generation of secondary flow is related to the coherent structure near wall especially that at corner. The turbulence interaction near adjacent wall tends to change the original coherent structure and results in the generation of secondary flow. Moreover, such turbulence interaction also changes the distribution of Reynolds stress at the cross section.

Besides the square duct, secondary flow can also been found in rectangular duct (Vinuesa et al. 2014, 2016), hexagonal duct (Marin et al., 2016), triangular duct (Hurst and Rapley, 1991), rounded square duct (Vidal et al., 2017), and so on while the characteristics of these secondary flows are different from each other due to different shape of the cross section. In this work, the geometry of the duct cross section is semi-circular and four vortexes are found near two corners (Larsson et al., 2011). Large Eddy Simulation (LES) was used to simulate the single-phase.

Regarding particle dispersion in turbulent flows, Friedlander and Johnstone (1957) studied small particle deposition in a flow with wall boundary by experiments, where the walls were coated with an adhesive glue to stop particles movement once they deposit on the wall. In this work, free-flight model was first proposed as that particles transported and carried by turbulent flows and gained enough inertia to slide through the viscous sublayer and then deposited. Based on this, more theories involving particle deposition were developed. McLaughlin (1989) further developed the free-flight model and concluded that deposition was mainly caused by free flight due to particle high deposition velocity. Later, Young and Leeming (1997) modelled the progress of particle deposition with 100% particle-wall collision probability and concluded that particle fluctuation near the wall is due to Brownian motion. In addition, particle mixing, dispersion and deposition has been widely investigated (McCoy and Hanratty, 1977; Wood, 1981). A Lagrangian Stochastic-Deterministic model of particle motion in turbulence was established (Milojević, 1990) in 1990. Recently, Park et al. (2017) proposed a simple subgrid model in Large Eddy Simulation (LES) to simulate isotropic particle-laden turbulence. In theory, although the energy involved in sub-grid eddies is much less than that involved in large eddies, sub-grid eddies still affect the particle behaviors. However, the subjects of this research are a large number of particles instead of single-particle. It is possible for sub-grid eddies to affect behaviors of single particle, but statistical laws are not changed. In statistical terms, large eddies with absolute advantage in energy are decisive factor of particle motion. So, lots of papers aimed to study particle behaviors in turbulent flows by point-particle model coupled with LES have been published, including studies of particle-laden flows with both large density ratio (Mallouppas and Wachem, 2013) and small density ratio (Ogholaja et al., 2018). It indicates the validity of this method.

Particle in isotropic turbulence has been widely investigated. Squires and Eaton (1990) studied the influence of turbulence on particle concentration by Direct Numerical Simulation (DNS) of isotropic turbulence and found that light particles preferentially distribute in regions with low vorticity and high strain rate. Kussin and Sommerfeld (2002) conducted an experimental study to review the effect of wall roughness on particle channel flow. Biferale et al. (2005); He et al. (2005); Kajishima (2004); Salazar et al. (2008); Vreman (2007) paid a lot effort to investigate particle rotation, separation and aggregation. Hadinoto and Curtis (2009) studied particle-laden turbulence at different Reynolds Numbers. The work (Burton and Eaton, 2005; Ferrante and Elghobashi, 2003; Portela and Oliemans, 2003; Schneiders et al., 2017) discovered the working mechanisms of the interaction between particle and turbulence. In recent years, some direct numerical simulations of particle motion in boundary layer have been carried out. For example, Sardina et al. (2012) studied turbophoresis effects in presence of various local Stokes numbers and found that the wall particle dynamics is dominated by the phenomenology of turbophoresis that is controlled by a viscous Stokes number varying at streamwise direction. Li et al. (2017) studied heavy solid particle dispersion in a spatially developing turbulent boundary layer over a flat plate and found that the spatial evolution of the particle wall concentration along the streamwise direction is similar to that of the mean skin-friction coefficient. In addition, some work has been carried out for particle motion in anisotropic turbulence. Winkler et al. (2006) studied the behavior of particles in a square duct, but the effect of gravity on particles was not considered. Yao and Fairweather (2010) studied particle distribution and resuspension at high Reynolds numbers as well as in a large range of particle size (Yao and Fairweather, 2012).

In this work, the flow Reynolds number is 80,000 and particles considered ranges in 10–500 μm with corresponding Stokes number 0.1–243. Particle dispersion in a semi-circular duct was studied. The flow field was simulated by Large Eddy Simulation and particle trajectory was computed by Lagrange tracking method taking account of gravity, buoyancy, drag force and lift force.

2. Mathematical model

2.1. Flow configuration

Simulations of the fully developed turbulent flow through a semi-circular duct were performed at a Reynold number based on bulk velocity and hydraulic diameter, namely $Re_b = 80{,}000$. The flow configuration is shown in Fig. 1, where spanwise, vertical, and streamwise directions are denoted as x, y, and z, respectively. The coordinate origin is set at the midpoint of the duct floor. The corresponding velocity components set at the (x, y, z) directions are (u, v, w). The angle between the curved ceiling and the straight floor is about 70° and the ceiling radius $r = 50$ mm. Other geometric dimensions are shown in Fig. 1. The hydraulic diameter of the duct $D_H = 42$ mm. Periodical conditions were imposed at the streamwise direction, where the computational domain length was set as $L_z = 4\pi D_H = 528$ mm. The duct length is sufficiently long to contain the streamwise-elongated, near-wall structures presented in wall-bounded shear flows. Such structures are rarely expected to be

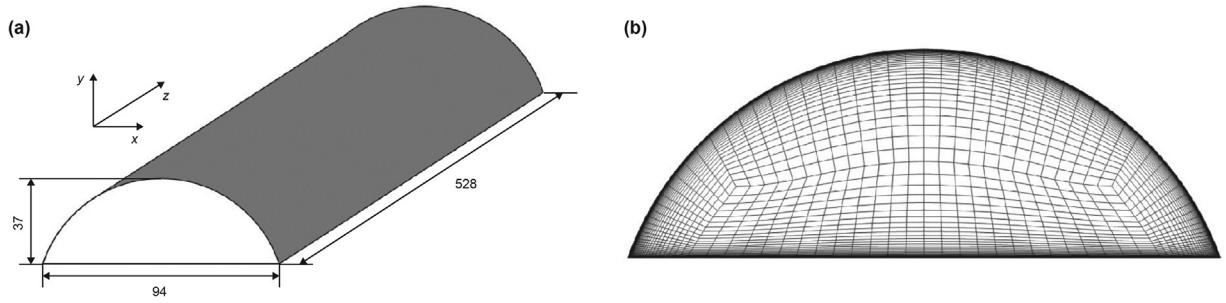

Fig. 1. (a) Schematic of computational domain (mm); (b) in-plane spectral element mesh considered in the case, with a total of 4080 elements in the *x*-*y* plane.

longer than approximately 1000 wall units (Rhie et al. 1983). The boundary conditions for the momentum equations were set as no-slip at the duct walls.

The physical domain was discretized using 7.18×10^5 grid points. All discretization was set uniformly at the streamwise (z) direction while at the spanwise (x) and vertical directions (y) grid points were set denser near the wall. The closest point to the wall was placed at x^+ or $y^+ = 1$. In this work "+" denotes inner scaling with the mean friction velocity $w_{\tau,\mathrm{m}}$ and the viscous length $l^* = \nu/w_{\tau,m}$. The flows investigated have bulk Reynolds number $Re_\mathrm{b} = w_\mathrm{b}D_\mathrm{H}/\nu$ as 80,000 and the equivalent friction Reynolds number $Re_\tau = w_{\tau,m}D_\mathrm{H}/\nu$ as 3528.

2.2. Large Eddy Simulation

In previous studies, the Reynolds Stress Model was used to simulate the semi-circular duct (Larsson et al., 2011). However, flow turbulence was not able to be obtained by this model due to its limitation. In order to obtain the turbulence of flow field, Large Eddy Simulation (LES) was developed to investigate the semi-circular duct. It is known that LES is able to provide temporary flow full information including the flow turbulence so it does not need to introduce approximate models to obtain transient velocity. It is known that LES separates large and small vortexes by filtering function, where large vortexes are directly simulated and small vortexes are closed by models (Js, 1963). In this work, the top-hat filter is adopted to filter vortexes at different scales (Germano, 1992). The continuity equation and momentum equation of incompressible, constant physical property, Newtonian fluid are listed as following.

$$\frac{\partial \overline{u}_j}{\partial x_j} = 0 \tag{1}$$

$$\frac{\partial \overline{u}_i}{\partial t} + \frac{\partial \overline{u}_i \partial \overline{u}_j}{\partial x_j} = -\frac{\partial \overline{p}/\rho}{\partial x_i} - \frac{\partial}{\partial x_j}\left(\overline{\sigma}_{ij} + \tau_{ij}\right) \tag{2}$$

In Eq. (2), $\overline{\sigma}_{ij} = -2\nu\overline{s}_{ij}$ is the kinematic viscous stress tensor and $\tau_{ij} = \overline{u_i u_j} - \overline{u}_i\overline{u}_j$ represents the effect of the sub-grid scale on the resolved scale. Such term is called as sub-grid scale stress and its solution is required to solve the filtered equations. The sub-grid scale stress model used in this work (Germano et al., 1991) represents the sub-grid scale stresses as the product of a sub-grid scale viscosity ν_{sg}, and the resolved part of the strain tensor ν_{sgs} evaluated as the product of the filter length Δ times an appropriate velocity scale, taken to be $\Delta \parallel \overline{s} \parallel$. The anisotropic part of the sub-grid scale stresses is given by Eq. (3).

$$\tau_{ij}^a = -2(C\Delta)^2 \parallel \overline{\boldsymbol{s}} \parallel \overline{s}_{ij}^a \tag{3}$$

which can be solved by applying a second filtering operation, denoted by ~, to Eq. (2). In the filtered equation, the sub-grid scale stresses can be shown as:

$$T_{ij} = \overline{u_i u_j} - \overline{u}_i\overline{u}_j \tag{4}$$

and then

$$L_{ij} = T_{ij} - \tilde{\tau}_{ij} = \overline{u}_i\overline{u}_j - \overline{u}_i\overline{u}_j \tag{5}$$

Such expression is known as the identity of Germano et al. (1991), and involves only resolved quantities. To evaluate C, some form of relationship between C and $C^2(\sim)$ at the grid-and test-filter levels must be specified. Based on the hypothesis that the cut-off length falls inside the inertial sub-range, the expression generally used is:

$$C^2 = C^2(\sim) \tag{6}$$

Such sub-range is not, however, guaranteed to occur in wall-bounded at low Reynolds numbers, where the largest deviations from universality of the sub-grid scale motions occurs in the weakest resolved strain. The model parameters at different filter levels are therefore proposed by Di Mare (2003).

$$C^2(\sim) = C^2\left(1 + \frac{\varepsilon}{2\sqrt{2}\Delta^{\sim 2} \parallel \overline{s} \parallel \parallel \overline{s}^a \parallel^2}\right) \tag{7}$$

where ε is the dissipation and assumed that the flow has length scale l and velocity scale v as

$$\varepsilon \approx v^3 \big/ D_\mathrm{H} \tag{8}$$

where v is bulk velocity and D_H is the hydraulic diameter of the semicircle duct.

Eq. (7) assumes that the scale of C can only be invoked if the cut-off falls inside an inertial sub-range, and when this occurs the modelled dissipation should represent the entire dissipation in the flow. Conversely, in the high Reynolds number limit, the dissipation is only determined by v and l, so that the ratio of ε to $\Delta^{\sim 2} \parallel \tilde{s} \parallel^3$ measures how far the flow is from scale preserving conditions. This equation is a first-order expansion of other scale-dependent expressions for C, which also use a single length and velocity scale (Porté-Agel et al., 2000). Eqs. (5) and (7), with contraction of both sides with the tensor ~ s, then give:

$$C^2 = \frac{2\sqrt{2}\left(C_*^2\Delta\right)^{\sim 2} \parallel \overline{\boldsymbol{s}} \parallel \parallel \overline{s}_{ij}^a \parallel^{\sim} \overline{s}_{ij}^a - L_{ij}^a \overline{s}_{ij}^a}{\varepsilon + 2\sqrt{2}\Delta^{\sim 2} \parallel \overline{s} \parallel \parallel \overline{s}_{ij}^a \parallel^2} \tag{9}$$

where C_*^2 is a provisional value for C^2, i.e., its value at the previous time step.

Computations were performed by using BOFFIN code that

implements an implicit finite-volume incompressible flow solver using a collocated variable storage arrangement. Fourth-order pressure smoothing is applied to prevent oscillations in the pressure field. The code has been used to investigate a wide range of flows (Bini and Jones, 2008; Di Mare and Jones, 2003; Yao and Fairweather, 2010, 2012).

2.3. Lagrangian particle tracking

Particle motion was modelled using Lagrangian approach. To simplify this problem considered, some assumptions were made as following. First, due to particle-laden flow being dilute, interactions between particles were ignored and the flow-particle was one-way coupled. Second, particle simulated was rigid sphere with the same diameter and density. Third, particle-wall collision was elastic. Based on these assumptions, the motion of a particle within the flow is governed by the following equation:

$$\frac{d\boldsymbol{V}_p}{dt} = \frac{3}{4}\frac{\rho}{\rho_p}\frac{C_D}{d_p}(\boldsymbol{V}-\boldsymbol{V}_p)|\boldsymbol{V}-\boldsymbol{V}_p| + (1-(\rho/\rho_p))\boldsymbol{g} + 1.615 d_p \mu Re_s^{0.5} c_{ls}\frac{[(\boldsymbol{V}-\boldsymbol{V}_p)\times\boldsymbol{\omega}]}{|\boldsymbol{\omega}|} \tag{10}$$

where $\boldsymbol{V}$ is the flow velocity and ρ the flow density, $\boldsymbol{V}_p$ is the particle velocity and ρ_p the particle density, d_p is the particle diameter, and g is gravity. $\boldsymbol{\omega} = \nabla \times \boldsymbol{V}$ is associated with the fluid rotation. Re_s is the particle Reynolds number in terms of shear flow, and $c_{ls} = \boldsymbol{F}_{ls}/\boldsymbol{F}_{ls,saff}$ represents the ratio of the extended lift force to the Saffman force (Saffman, 1968) as following.

$$c_{ls} = \begin{cases} 0.0524(\beta Re_p)^{0.5} & \text{for } Re_p > 40 \\ \left(1-0.3314\beta^{0.5}\right)e^{-Re_p/10} + 0.3314\beta^{0.5} \end{cases} \tag{11}$$

where $\beta = 0.5Re_s/Re_p$, C_D is the Stokes coefficient for drag$C_D = (1+0.15Re_p^{0.687})\cdot 24/Re_p$ and Re_p is the particle Reynolds number $Re_p = d_p|\boldsymbol{V}-\boldsymbol{V}_p|/\nu$. The last term on the right-hand side of Eq. (10) is slip-shear force.

In this paper, only Stokes drag, gravity, buoyancy and lift force are considered. The drag force is the main strength dominating particle behavior in the flows as shown in Zhao et al. (2020). Due to particle-wall impaction, electrostatic charge can be generated at the particle surface and the duct wall (Yao et al., 2004). In this work the duct considered was set at horizontal level and electrostatic force generated was confirmed to be much lower than the gravity by at least two orders of magnitude (Yao et al., 2006). In addition, Hydrostatic force, Magnus force, Basset force and additional mass force are ignored because they are much smaller than the forces considered (Armenio and Fiorotto, 2001). Their study found that the effect of these forces on particle dispersion is only about 1% even for small density ratios.

The fourth order Runge-Kutta method was used to solve the particle motion equation (Eq. (10)). Particles were randomly distributed throughout the duct at the initial condition, and the initial particle velocity was equal to the local flow velocity. Periodic boundary condition was set as that particles leaving the outlet were reintroduced into the inlet. The particle field is solved by the code written by ourselves.

Particle and fluid densities were set as $\rho_p = 2500$ kg/m^3 and $\rho = 1000$ kg/m^3, respectively. The fluid kinematic viscosity $\nu = 1.004 \times 10^{-6}$. Particle diameter $d_p = 10, 50, 100, 500$ μm and $St = 0.10, 2.43, 9.72, 243.05$, respectively. The total number of particles simulated is 10^3-10^4 given that the statistical properties of the particles irrelevant to the number of particles. Other parameters are shown in Table 1.

3. Results and discussion

3.1. Flow field analysis

To verify the accuracy of the proposed simulation approach and the numerical solution method used, LES results of the fully developed turbulent flow in a semi-circular were compared with experimental data and RMS solutions (Larsson et al., 2011), as shown in Fig. 2. Four profiles for spanwise mean velocity are compared. The solid and dotted profiles present the current simulation and Larsson's simulation (Larsson et al., 2011), respectively. The points represent Larsson's experimental results (Larsson et al., 2011). It is seen that current simulations agree well with other works, which indicates that the simulation method used is adapted to this study.

The contours of the streamwise mean velocity and vectors of the secondary flow in the right half of the semi-circular duct are shown in Fig. 3. Such secondary flow in a semi-circular duct have been demonstrated by Larsson et al. (2011) experiments. Similar to the secondary flow in the square duct, that in the semi-circular duct is found to move from the center to corners and then return to the center along walls. The ceiling of the semi-circular duct is inward and two counter-rotating vortices formed in the corner are tangent at the diagonal, which causes the vortices near the ceiling wall occupy less space. The diagonal is the bisector of the angle between the ceiling tangent at the corner and the floor. In Fig. 3b, it is shown that similar to the square duct flow the secondary flow causes the contours of streamwise velocity to distort slightly and bulge towards the corner. It is found that the contours near the ceiling are parallel to the wall. This is because the secondary flow near the ceiling is always parallel to the wall.

It is known that secondary flows are related to flow fluctuations. That is, the corner is not a sufficient condition for the secondary flow. Larsson et al. (2011) proved that the secondary flow cannot be obtained by isotropic turbulence model. As such the generation of the secondary flow is related to the geometric shape of duct as well as the fluctuation and anisotropy of turbulence. Turbulence in a semicircular duct becomes one of the necessary conditions for secondary flow generation. The generation mechanism of the secondary flow is proposed by Huser and Biringen (1993) as that the flow fluctuation is so strong near wall that presents distinctive structures as jets and sweeps. Such bursting behaviors are related to the characteristics of the boundary layer near wall. The wall direction determines the boundary layer direction and the turbulence structure direction there (near the wall). As two walls cross and form a corner, the bursting behaviors near them tend to interact with each other. For a single wall, the bursting behavior presents as a jet because there is no fluid mass beyond the end of the wall and the flow can move perpendicularly to the wall. For two walls, the ejection behavior induces at the end of two walls separately and interacts at the corner, which forms the secondary flow. In the end, due to the effect of continuity, the fluid moves toward the corner and shape the secondary flow.

Table 1
Parameters used in the simulations of particle dispersion.

d_p, um	d_p^+	St (τ_p^+)	τ_p, s	Gravity-buoyancy, N
10	0.84	0.10	1.38×10^{-5}	7.70×10^{-12}
50	4.20	2.43	3.46×10^{-4}	9.63×10^{-10}
100	8.40	9.72	1.38×10^{-3}	7.70×10^{-9}
500	41.98	243.05	3.46×10^{-2}	9.63×10^{-7}

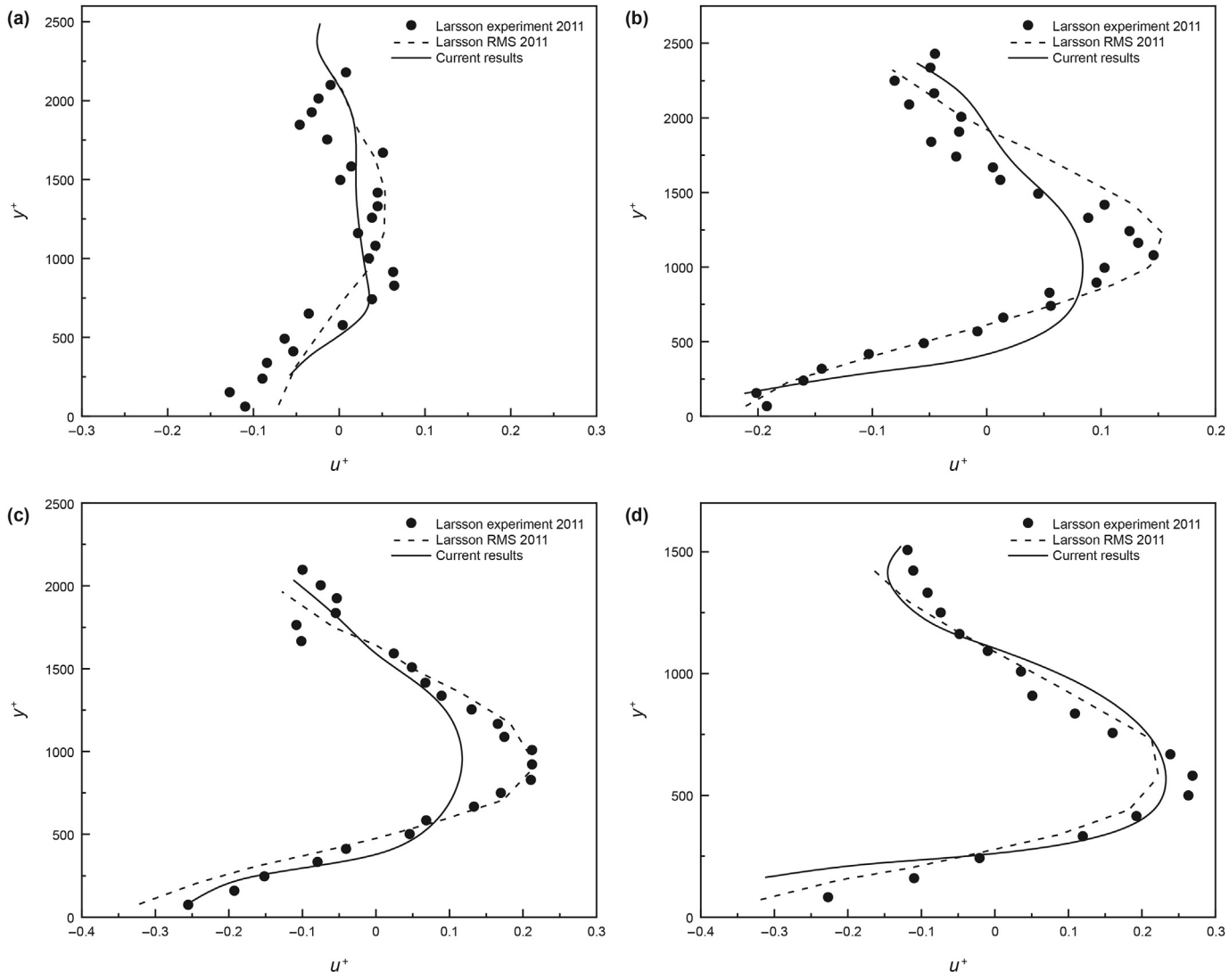

Fig. 2. Velocity profiles, simulation vs. experimental data for (a) $x = 0.1r$, (b)$x = 0.3r$, (c) $x = 0.5r$ and (d) $x = 0.7r$.

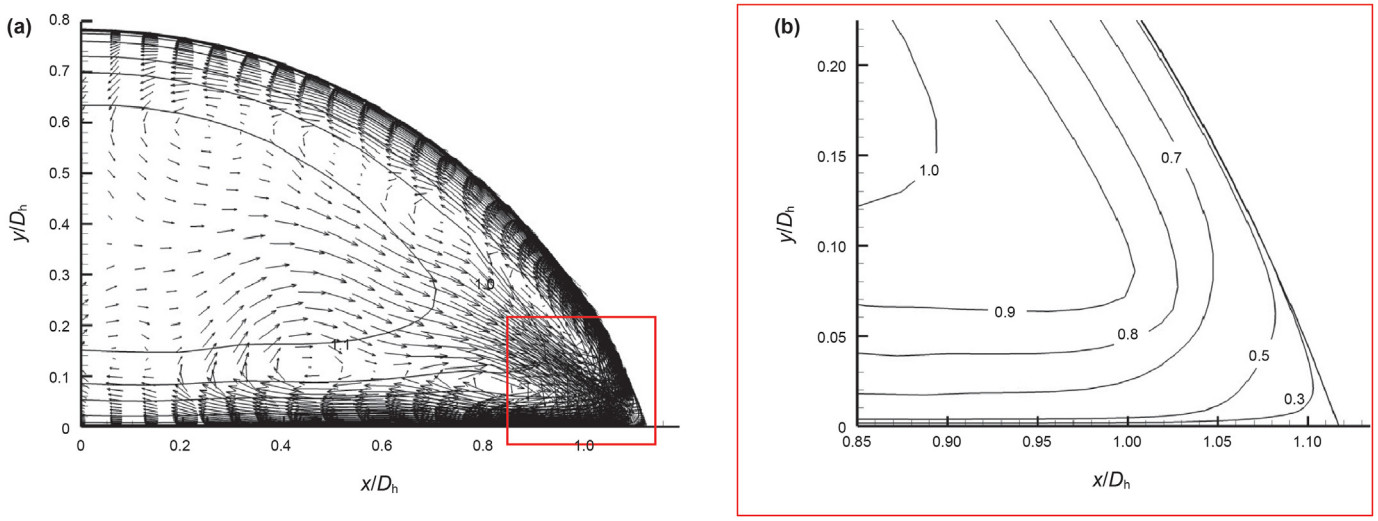

Fig. 3. a Streamwise mean velocity contours and the secondary flow vectors, b the contours near the corner (red box in Fig. 3a).

Regarding the semi-circular duct, the obvious difference from other flows is the geometrical structure, where a straight wall meets with an arc wall. Based on the analysis of the born mechanism of a secondary flow, it is believed that the secondary flows tend to be formed at corners in the semi-circular duct. Two vortices near the corner distribute symmetrically along the angular bisector. The secondary flow generates at a corner and two vortices occupy the entire sections. In the semi-circular duct flow, at the corner, the area between the curved wall and the angular bisector is much smaller than the area between the straight floor and the angular bisector. As such, the vortex generated near the curved wall is restricted in a smaller space, and the size of the secondary flow is smaller than that generated near the straight floor under the angular bisector. In short, the secondary formed in the semi-circular duct is asymmetric.

Generally, the secondary flow formed in a semi-circular duct is similar to that formed in a square duct as both originate from the corner. The angle of the corner determines the boundary between the adjacent secondary flow vortices. The geometry of the walls does not much affect the boundary between the adjacent vortices. In Figs. 3 and 4, it is seen that at the center-plane the flow contours do not deform significantly indicating that the secondary flow at the center-plane is weak. Fig. 4 shows the contour of the secondary flow $\sqrt{u^2+v^2}$, which is normalized by the bulk velocity w_b. It is seen that the highest energetic region (in red) of the secondary flow locates between the straight floor and the corner diagonal while the lowest energy level is near the ceiling. The burst events lead the secondary flow to occur near the wall and its maximum magnitude is found near the floor. In addition, the ceiling curvature reduces the effect of injection on the flow that makes the magnitude of the secondary flow near the ceiling smaller. The magnitude of the maximum secondary flow is about 2% of the bulk velocity, which is similar to that in the square duct. In addition, it is found that the general distribution of the secondary flow in a semi-circular duct is similar to that in a square duct. However, the difference between the semi-circular duct and the square duct is that the secondary flow in a corner of the semi-circular duct is not symmetrical along the diagonal. One branch of the secondary flow near the curve wall is smaller than the other one near the straight floor indicating that the curve wall tends to inhibit the secondary flow. It is suggested that wall bending inward not only limits the space occupied by vortex but also reduces the intensity of the secondary flow. The latter may be related to decreasing the space at the normal direction of the ceiling.

Fig. 5 is the contours of the turbulent kinetic energy ($(\overline{u'^2}+\overline{v'^2}+\overline{w'^2})/w_b^2$), where the secondary flow is found to have a significant effect on it. The maximum turbulent kinetic energy appears near the ceiling and floor, while the local minimum presents at the center section of the semi-circular duct and the global minimum presents at the corners. It indicates that the turbulent fluctuations are very strong near the wall because momentum exchange there. On the other hand, the turbulent kinetic energy is minimum at the corner under the effect of the adjacent walls, which decreases wall shear stress and turbulent fluctuation.

Contours of the Reynolds shear stresses $\overline{uw}^+$, $\overline{vw}^+$, and $\overline{uv}^+$, scaled by $w_{\tau,m}$, are shown in Fig. 6. Reynolds stress component $\overline{uw}^+$ (Fig. 6a) is high near the ceiling wall and $\overline{vw}^+$ is high at the top ceiling and the floor bottom, which is similar to the turbulence generated in a square duct. Regarding the square duct turbulence, Marin et al. (2016) reported that the values of $\overline{uw}^+$ and $\overline{vw}^+$ are fairly high near the vertical and horizontal walls respectively, which may be due to the transportation of normal turbulence in boundary layer. So it can be deduced that the region with the highest $\overline{uw}^+$ and $\overline{vw}^+$ in the semicircular duct is independent of the secondary flow. In the region below the diagonal (as shown in the red box in Fig. 6a), $\overline{uw}^+$ reaches the local maximum level and causes the secondary flow near the floor. Similarly, $\overline{vw}^+$ reaches the local maximum above the diagonal and its direction is opposite to that near the floor. The same conclusion can be obtained for $\overline{vw}^+$ at the top. Therefore, in Fig. 6b, the region in red boxes may be related to the generation of secondary flows near the ceiling. In a square duct, it is known that $\overline{uv}^+$ is high along the diagonal, which can be also found in a semi-circular duct. It causes the secondary flow to move from the center to corners. Furthermore, the maximum $\overline{uv}^+$ in the semi-circular duct is found near the ceiling, which causes transportation of wall-normal turbulence in the boundary layer. Therefore, it can be concluded that the distribution of Reynolds shear stresses in a semi-circular duct is quite similar to that in a square duct.

Regarding the flow field near the floor in a semi-circular duct, the profiles of streamwise velocity, spanwise and vertical fluctuations at the four lines $x = 0.1r$, $x = 0.3r$, $x = 0.5r$ and $x = 0.7r$ are shown in Fig. 7a–c, respectively. It is seen that the profiles of streamwise mean velocity (Fig. 7a) at the four positions is very close and the velocity near the center plane is slightly larger than that near the corner. This is because the flow near the corner is restricted by its adjacent walls. It is obtained that the velocity is linear $y^+ < 15$ but logarithmic $y^+ > 15$.

Fig. 7b and c shows the root mean square of the spanwise and the vertical fluctuation, respectively. It is seen that the spanwise fluctuation (Fig. 7b) decreases gradually from the center ($x = 0.1r$) to the corner ($x = 0.7r$), while the vertical fluctuation (Fig. 7c) at different positions is very close. In addition, it can be found that

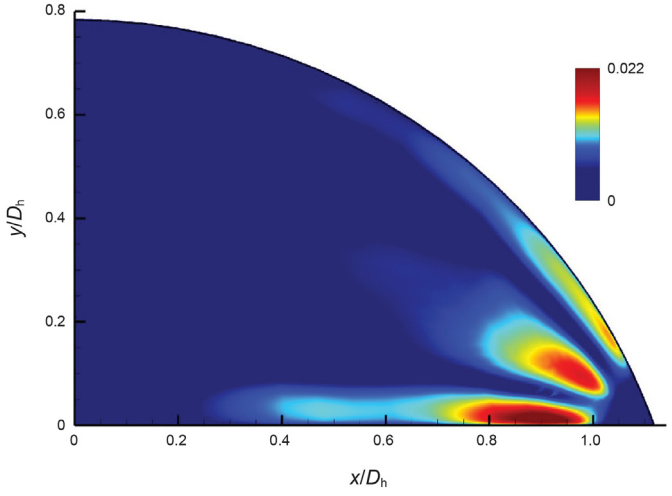

Fig. 4. Secondary flow ($\sqrt{u^2+v^2}/w_b$) contours.

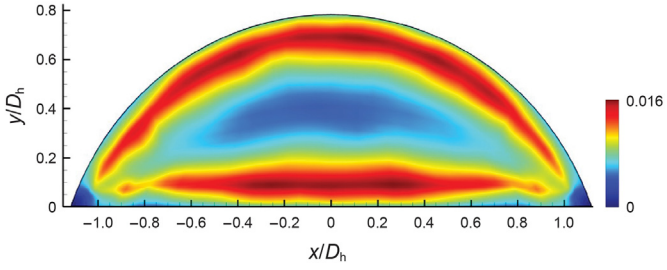

Fig. 5. Contours of turbulent kinetic energy, $(\overline{u'^2}+\overline{v'^2}+\overline{w'^2})/w_b^2$

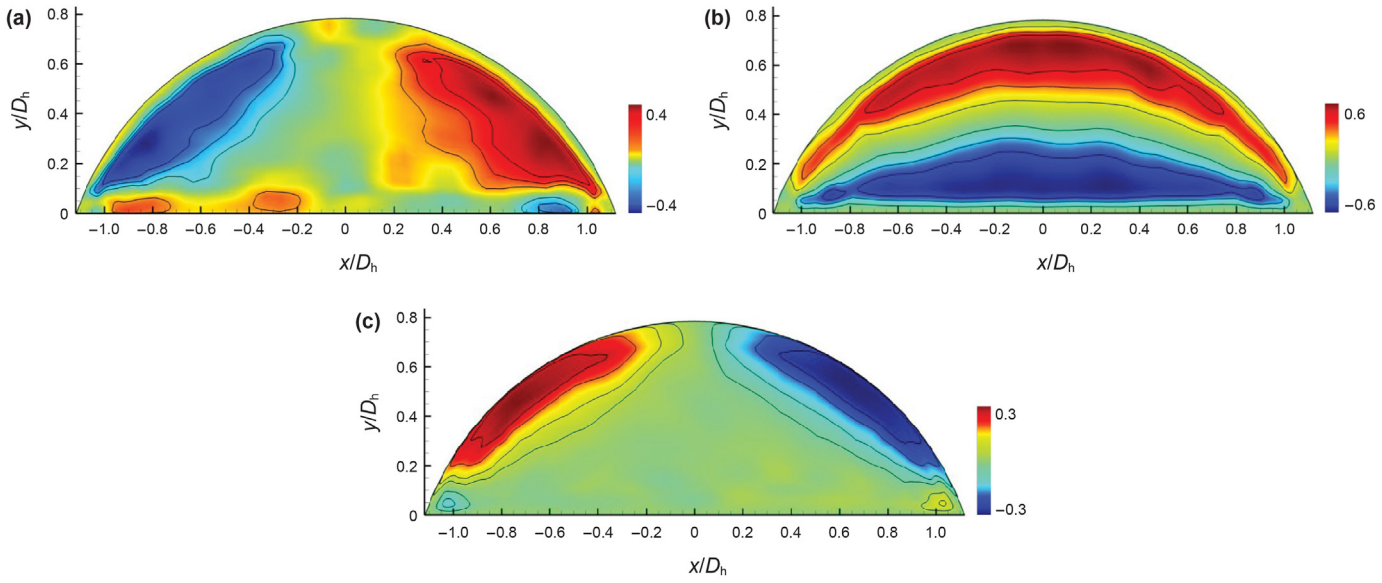

Fig. 6. Reynolds stress tensor components (a) $\overline{uw}^+$, (b) $\overline{vw}^+$, (c) $\overline{uv}^+$, normalized with $w_{\tau,m}$.

spanwise fluctuations (Fig. 7b) rise faster than vertical velocity fluctuations (Fig. 7c). This is because that the fluid motion is less constrained by the floor at the spanwise direction in comparison with the vertical motion. As such, due to constrain effect, the velocity and fluctuation of the flow near floor is relatively small at the vertical direction.

3.2. Particle field analysis

To investigate particle distribution, the cross section of a semi-circular duct was divided into many square cells with the same size as side length $l^+_{\text{cell}} = 140$. The distribution density of particles called '*den*' can be calculated as Eq. (12), where N_{cell} and N represent the number of particles in a cell and in the whole region, respectively, A_{cell} and A represent the area of a cell and that of the duct cross section, respectively.

$$den = \frac{N_{\text{cell}}/A_{\text{cell}}}{N/A} \tag{12}$$

Contours of particle distribution density in the cross section are shown in Fig. 8. It is seen that the smallest particle (d_p = 10 μm, Fig. 8a) evenly distribute in the whole duct and none found deposit on the floor while some of them like to preferentially distribute near the ceiling in a small region (as shown in red box in Fig. 8a). Larger particles (d_p = 50,100,500 μm) tend to most deposit at the center of the duct (as marked in red in Fig. 8) and little of them concentrate at the corner. Among them, the particles with $d_p = 50$ μm (Fig. 8b) are evenly distributed in the center of the duct. However, particles with d_p = 100 μm (Fig. 8c) are obviously distributed in the lower part of the duct, and the largest particles ($d_p = 500$ μm) (Fig. 8d) are completely deposited on the duct floor in the same period of time.

In addition, it is found that the distribution of particles varies with particle size at the corners. For example, the smallest particles ($d_p = 10$ μm, Fig. 8a) tend to have the same distribution density at the corners as that at the duct center. However, for larger particles (d_p = 50,100,500 μm, Fig. 8b–d), their distribution densities at the corners are obviously higher than that at the duct center. This may be because that the flows at the corners have so low momentum that cannot put particles back to the duct center. On the other hand, it is known that fluctuation is more likely to affect small particles than large ones. Table 1 shows that the relaxation time of 100 um particle is 10^{-3} s and smaller particles have shorter relaxation time. The relaxation time of 500 μm particle is 10^{-2} s and its movement less affected by the flow fluctuation in this period (10^{-2} s) because such large particle tends to deposit on floor in less 10^{-2} s.

Figs. 9 and 10 show the contours of particle velocity at the spanwise and vertical direction, respectively. The values of contours are the averaged velocities of particles in cells. It is seen that the distribution of particle velocity is consistent with that of secondary flow. In Fig. 9, the distribution of particle spanwise velocity ('u_p') can be roughly divided into three regions as ceiling area (Region 1), diagonal area (Region 2) and floor area (Region 3). In Regions 1 and 3 particles tend to move toward the duct center while in Region 2 they like to move toward the corners, which is independent of particle size. For particle $d_p = 10$ μm, particle velocity u_p in Region 2 is significantly larger than other regions but for other larger particles, their velocities tend to distribute uniformly in three regions. This is due to the inertial effect on particles. In Fig. 10, the distribution of particle vertical velocity $\boldsymbol{V}_p$ can be divided into four regions at the cross section. In Regions 1, 2 and 3, particles movement is dominated by the secondary flows while in Region 4 due to secondary flow becoming less particles movement is dominated by gravity. These four regions can be shown more clearly for smaller particles due to their better flow ability. In Figs. 9 and 10, the contours of particle velocity show that small particles ($d_p < 100$ μm) tend to move with the secondary flows at the cross section, and distribute in the whole section under the effect of flow fluctuation. It is seen that the effect of secondary flow is more significant to dominate particle behavior than that of flow fluctuation. This may be caused by the fact that the magnitude of the fluctuation is much smaller than that of the averaged velocity.

Fig. 11 shows the scatter plot of particle spanwise velocity u_p. It is seen that u_p is fairly low near walls ($x^+ > 3500$ or $x^+ < -3500$) and well distributed in the center region. u_p tends to approach 0 with increasing particle size. This is because more and more particles tend to deposit on the bottom floor with increasing particle size under gravity effect. In Fig. 11, it is seen that all sized particles have the highest velocity near center region ($x^+ = 0$) with

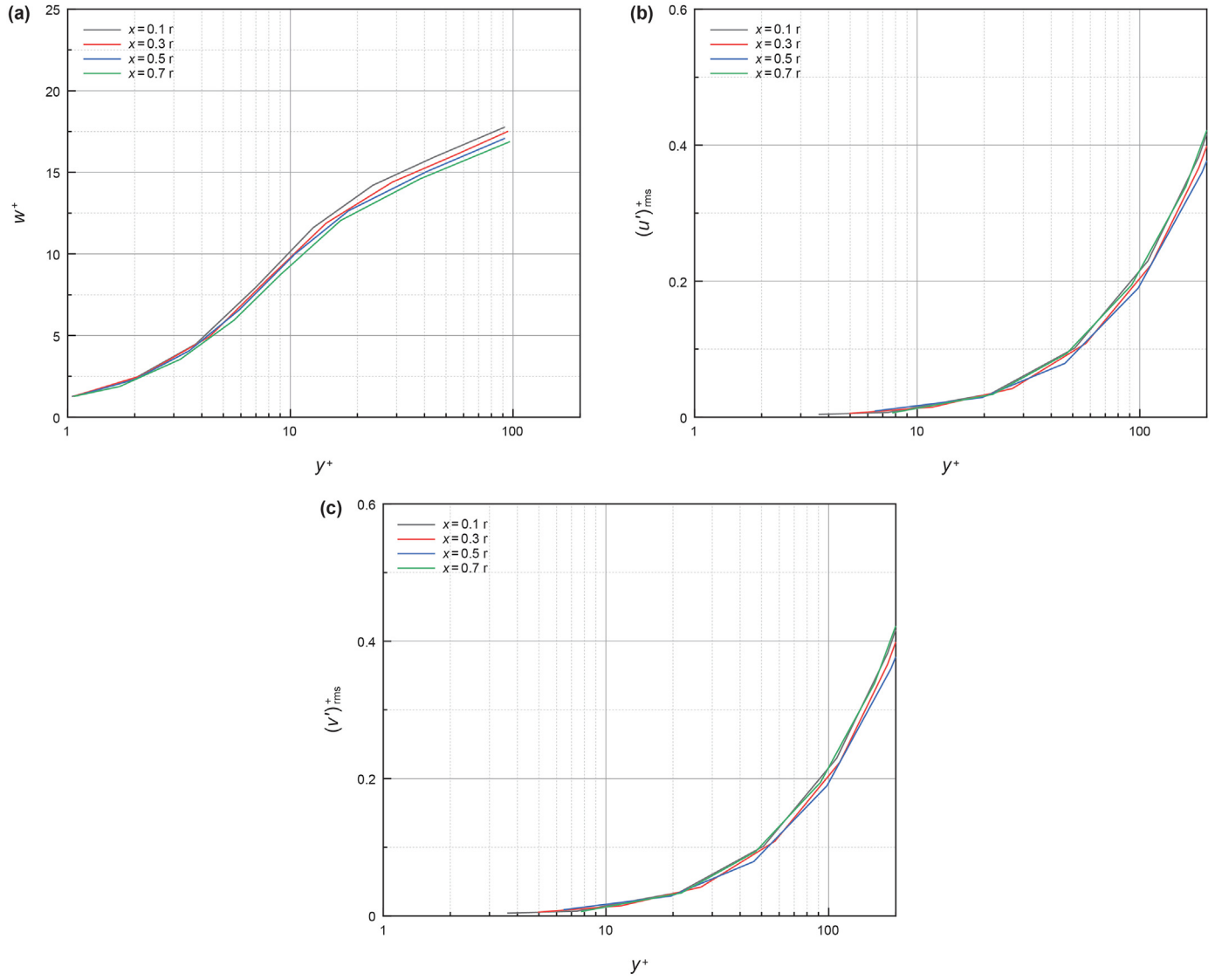

Fig. 7. Inner-scaled turbulence statistics. a streamwise velocity, b spanwise fluctuations, c vertical fluctuations.

the widest velocity distribution while lower velocity near the corners ($x^+ > 3500$ or $x^+ < -3500$) with the narrower velocity distribution. This may be caused by the secondary flow. Furthermore, Fig. 11d shows that at the same moment most particles with 500 μm tend to deposit at the bottom floor, where most of them distribute near floor center and few of them near corners ($x^+ > 3500$ or $x^+ < -3500$). It is suggested that particles with 500 μm tend to move toward the floor center as they deposit at the floor. It can be verified by another fact as shown in Fig. 11d. In the right zoom window in Fig. 11d, it is seen that the distribution of particle velocity concerns at two regions as $u_p > 0$ in $x^+<0$ and $u_p < 0$ in $x^+ > 0$, which confirms that particles tend to move from corners to the duct center. It is the secondary flow that causes particle concentration. In addition, as shown in Figs. 9 and 10, the larger particles the higher the maximum particle velocity (except of 500 μm particle). This may be related to the relaxation time because the larger particle the longer relaxation time indicating more interaction caused by the flow.

Fig. 12 shows drag force acting on particles sized from 10 to 100 μm, where the drag force is obtained by averaging the drag forces acting on all particles in a single cell. In Fig. 12a, 10 um particle, the drag force is most shown vertically upward near wall, but becomes chaos at the duct center, which may be caused by the secondary flow. Under the effect of the secondary flow, particles tend to move irregularly and disperse well in the whole duct. However, near the wall, the fluid velocity is lower, and the main function of the drag force is to counteract the gravity. The effect of the secondary flow on the particle behavior decreases with increasing particle size due to gravity. In addition, the drag force acting on the 10 μm (Fig. 12 a) particles looks more complex than that on larger particles (Fig. 12b and c).

Similarly, Fig. 13 shows lift force acting on particles. As particle diameter is larger than 100 μm it tends to deposit on floor in a short time under gravity effect. As such, for smaller particles with diameter of 10 μm and 50 μm lift force acting on particles is shown in Fig. 13. As shown in Eq. 10, the lift force is related to the fluid velocity difference between two sides of a particle. The larger particle the higher difference of flow velocity between two sides so the higher the lift force. It is shown that lift force acting on the 10 μm particles is near 0 because the particle is so small that the velocities between its two sides differ little. On the other hand, the flow fluctuations also cause lift force due to its difference between

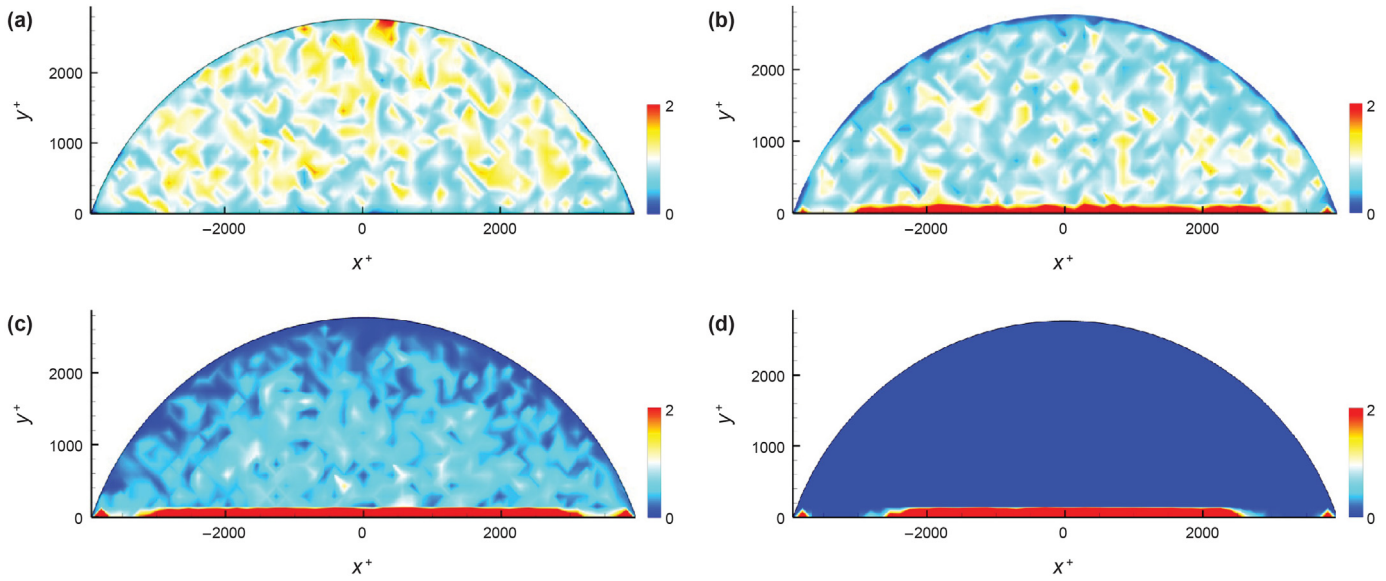

Fig. 8. The distribution density of particles in a semicircle duct, (a) $d_p = 10$ μm, (b) $d_p = 50$ μm, (c) $d_p = 100$ μm, (d) $d_p = 500$ μm, $t^+ = 21{,}127$.

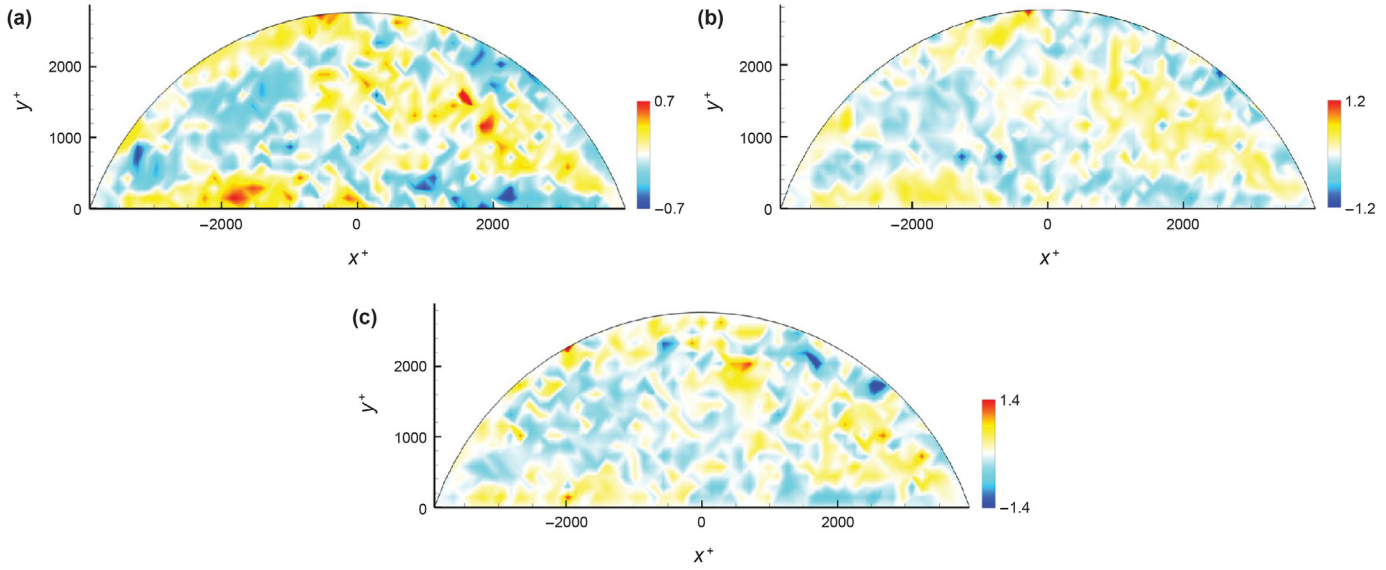

Fig. 9. Contours of particle spanwise velocity, normalized with $w_{\tau,m}$, (a) $d_p = 10$ μm, (b) $d_p = 50$ μm, (c) $d_p = 100$ μm, $t^+ = 21{,}127$.

particle both sides. For 10 μm particles, the effect from the flow fluctuations on particles behavior is also from lift force. As shown in Fig. 13a, the lift force presents disorder. As particle increases the difference of flow velocity between two sides of this particle becomes larger, which improves the lift force. It can be verified by Fig. 13b in comparison with Fig. 13a.

It is well known that lift force is related to the slip velocity and fluid velocity gradient at the particle position. In the boundary layer, the velocity gradient of the fluid is very large, and the lift force on the particles cannot be ignored. When the linear velocity of the particles in the duct is greater than that of the fluid, the lift force causes the particles to approach the wall. Conversely, the lift force causes the particles to move away from the wall. Therefore, as Wang et al. (1997) found, if the inertia of the particles is sufficient to generate slip velocity, the lift force will cause more particles to deposit towards the wall. As shown in Fig. 13, this phenomenon can also be seen in current results. Nevertheless, the magnitude of the lift force is much smaller than the drag force (Figs. 12 and 13), and its contribution to particle deposition is weak.

Further analysis of lift force reveals that it does not always point towards the wall. This may have something to do with varying instantaneous slip velocities. So, for a single particle and certain position, lift force can either keep particles away from the wall or near the wall. For a large number of particles, lift force makes most particles close to the wall and increase the deposition rate.

The Probability Density Function (PDF) of particles near the floor ($y^+ < 42$) is shown in Fig. 14. It is seen that the smaller particles are more evenly distributed near the floor and the larger particles are more concentrated at the floor center, which may be explained by following facts. First, small particles are most dominated by the drag force and tend to be evenly distributed throughout the duct. In contrast, due to gravity effect large particles tend to deposit at the floor quickly and move toward the floor center under the effect of the secondary flow (as shown in Fig. 11). Second, near the duct floor,

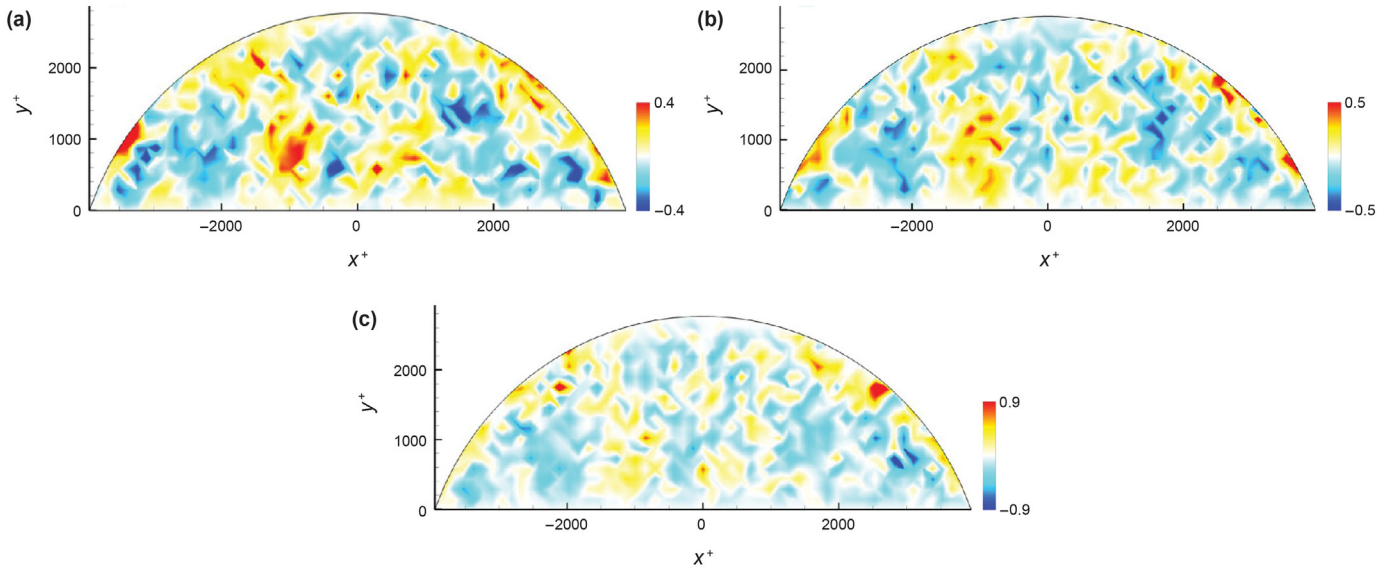

Fig. 10. Contours of particle vertical velocity, normalized with $w_{\tau,m}$, (a) $d_p = 10$ μm, (b) $d_p = 50$ μm, (c) $d_p = 100$ μm, $t^+ = 21{,}127$.

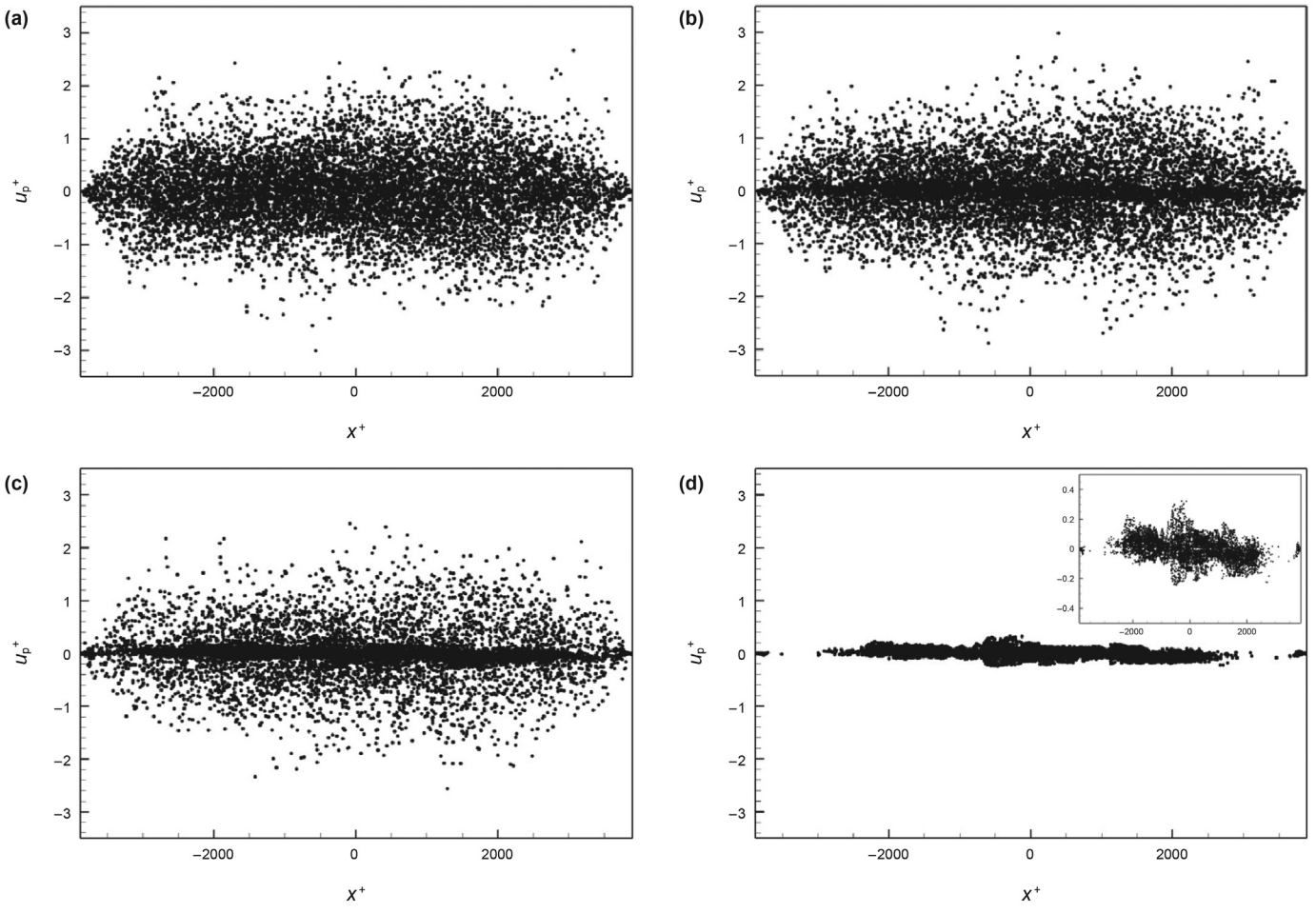

Fig. 11. Scatter plots of particle spanwise velocity, (a) $d_p = 10$ μm, (b) $d_p = 50$ μm, (c) $d_p = 100$ μm, (d) $d_p = 500$ μm, $t^+ = 21{,}127$.

secondary flows move from corner to center. Under its effect, large particles deposited near the floor tend to move toward the floor center. For example, as shown in Figs. 14b and 50 μm particle has an obviously higher PDF near the floor center. Such trend increases with particle size and working time. On the other hand, small particles tend to slightly accumulate at corners (as shown in

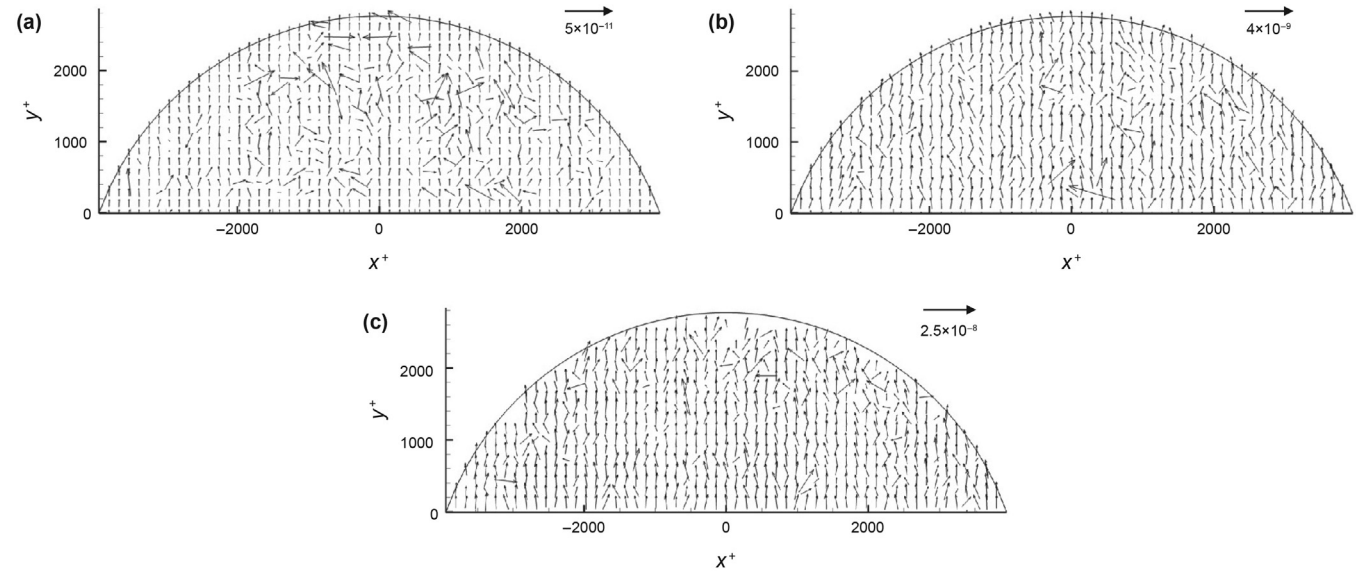

Fig. 12. Drag force vectors(N), (a) $d_p = 10$ μm, (b) $d_p = 50$ μm, (c) $d_p = 100$ μm, $t^+ = 21{,}127$.

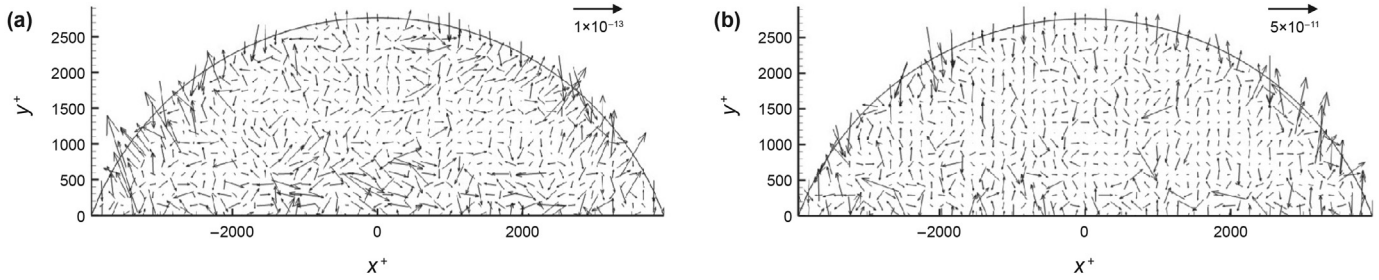

Fig. 13. Lift force(N), (a) $d_p = 10$ μm, (b) $d_p = 50$ μm, $t^+ = 21{,}127$.

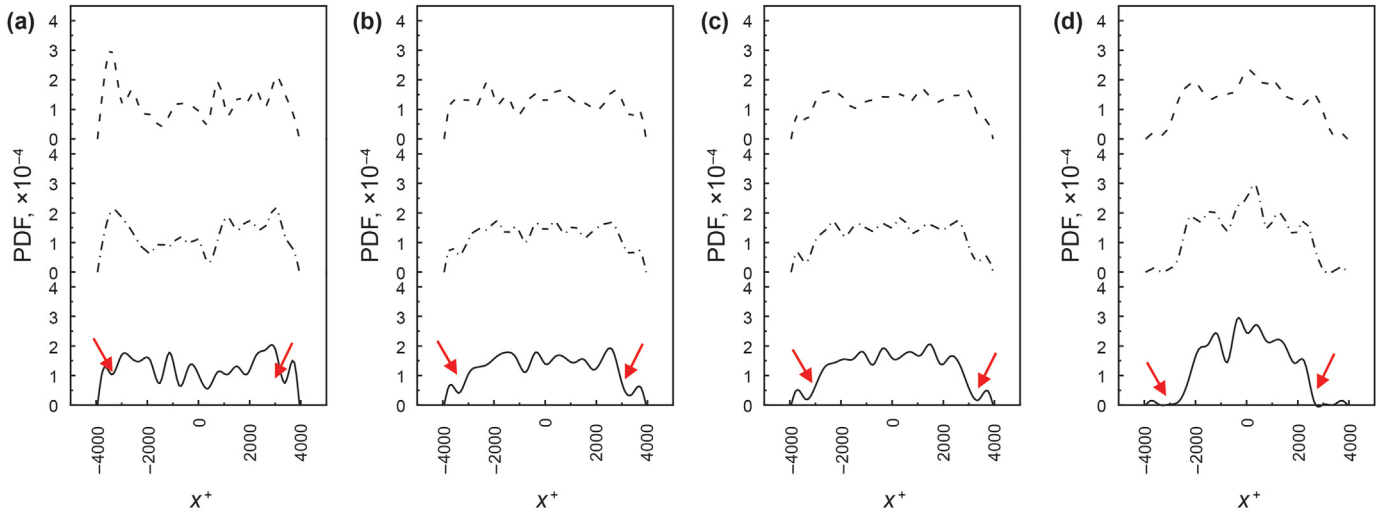

Fig. 14. Probability density function (PDF) of particles near the floor ($y^+ < 42$), d_p = (a) 10 μm, (b) 50 μm, (c) 100 μm, (d) 500 μm. From top to bottom, $t^+ = 7042$, 14,082, 21,127, respectively.

Fig. 14a) due to the secondary flow moving from the duct center to the corners. Particle PDF at the corner decreases with increasing particle size due to gravity effect. In short, the behavior of smaller particles is dominated by the drag force (secondary flow) with their trajectories from the duct center toward corners, while that of larger particles is dominated by gravity because they tend to deposit to wall quickly and move toward the floor center under the secondary flow effect.

In Fig. 14, there are a low PDF appeared around $x^+ = \pm 3500$ for all cases, which may be due to the effect of the secondary flow. Small particles tend to distribute throughout the duct including moving from the semi-circular duct center to the corner and from the corner to the floor center. However, for large particles as $d_p = 500$ μm, they tend to deposit on the floor and concern at the floor center under the effect of the secondary flow as analyzed above so that PDF around $x^+ = \pm 3500$ is near 0.

Fig. 15 shows the instantaneous distribution of particles with various diameters ($d_p = 50$,100,500 μm) on the floor ($y^+ < 42$). It is seen that 50,100 μm particles (Fig. 15a and b) randomly distribute on the floor. As $d_p = 500$ μm (Fig. 15c), distinct streaks of particle distribution can be found on the floor where the flow field is found to be interlaced with high speed streaks and low speed streaks (Fig. 15d). Large particles (500 μm) tend to deposit on the floor quickly and their distribution is dominated by local turbulence of the flow field near the floor. High and low speed streaks near the floor act on large particles deposited and make them distribute as streaks. In addition, ribbons can be found Fig. 15d between corner and center with little particles. It is consistent with that found in Fig. 14 where PDF appears concave around $x^+ = \pm 3500$.

Fig. 16 shows PDF of particles near the ceiling, where the distance between particle and ceiling is $\Delta^+ \leq 42$. As shown in Fig. 16a, O is the circle center with $\theta = 0$ and the duct corners locate at $\theta = \pm 70.1°$. In Fig. 16b, the distribution of 10 μm particles near the ceiling is significantly different from other larger particles (shown in Fig. 16c and d). It is seen that in Fig. 16b the maximum of particle PDF occurs around the ceiling center. This is because that under the effect of the secondary flow particles tend to concentrate at ceiling centre and move upward. However, at the duct top secondary flow become so weak that particles hardly approach there. For particle 50 μm (Fig. 16c), they tend to be pulled away from the duct top by gravity. Few of them enter this region and stay there under the effect of the secondary flow. For particle 100 μm (Fig. 16 d), there is no such particle found in this region.

Figs. 14–16 shows the distribution of particles near the wall and corner. In the central region of the duct, particles disperse freely under the effect of drag force and gravity. Near the wall region,

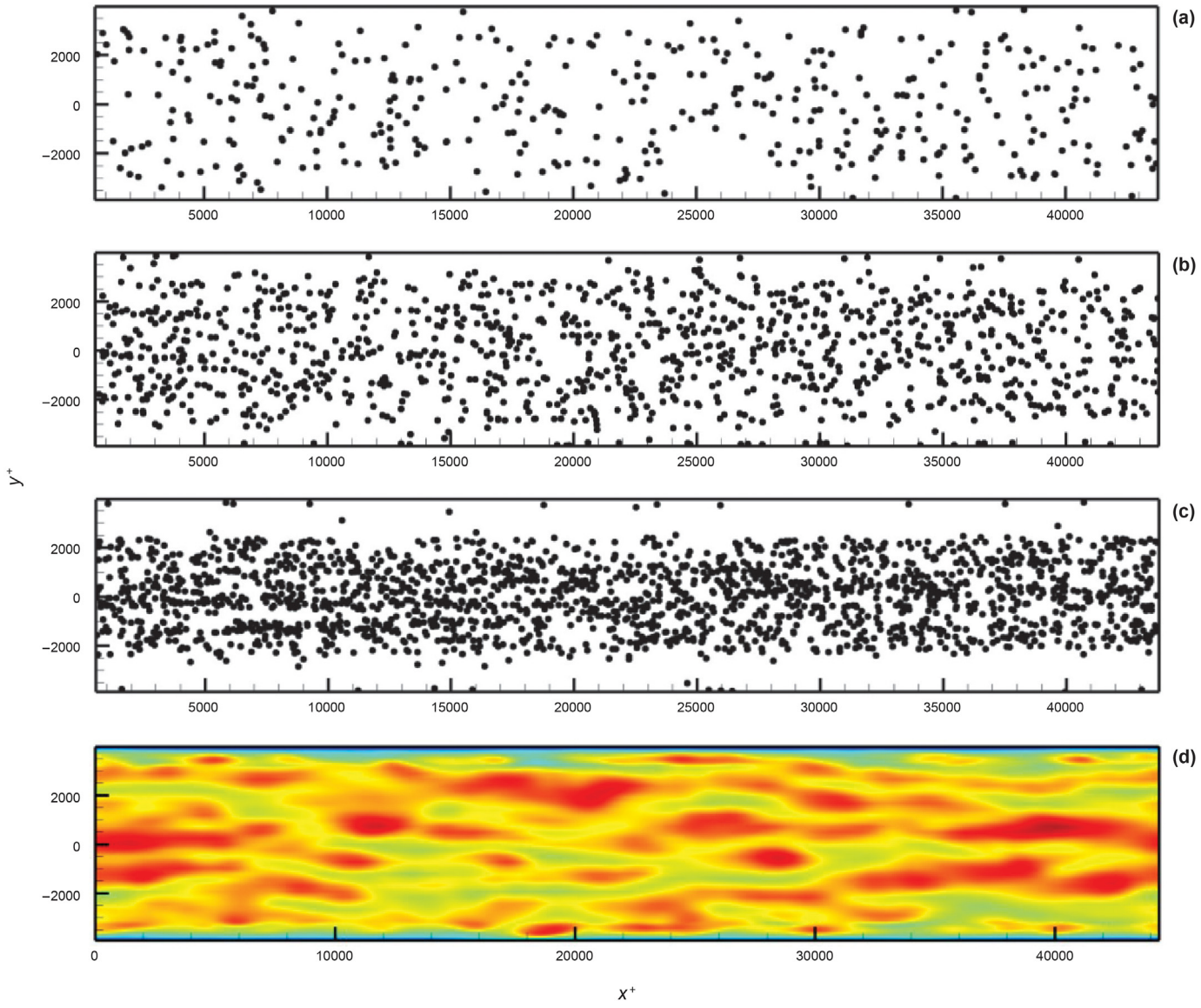

Fig. 15. Instantaneous distribution of particles near floor ($y^+ < 42$), d_p = (a) 50 μm, (b) 100 μm, (c) 500 μm and (d) instantaneous velocity contours, $y^+ = 42$, $t^+ = 21{,}127$.

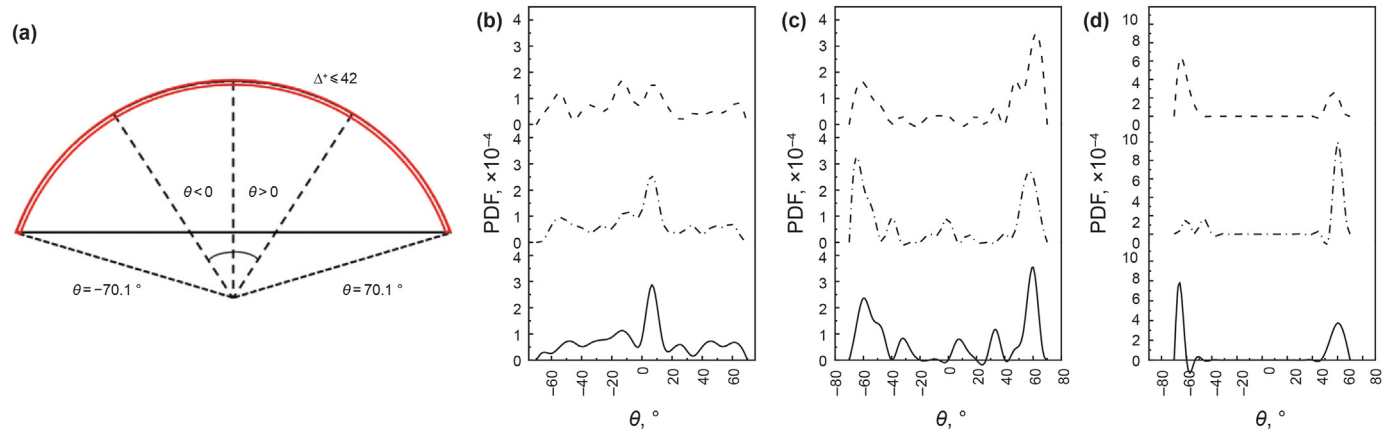

Fig. 16. (a) Probability density distribution function (PDF) of particles near the ceiling ($\Delta^+ \leq 42$), $d_p =$ (b) 10 μm, (c) 50 μm, (d) 100 μm. From top to bottom, $t^+ = 7042$, 14,082, 21,127, respectively.

particle movement is not only affected by drag force and gravity but also by the wall. For example, for particles 50–500 μm as deposit on the floor, they tend to move toward the floor center under the effect of secondary flow (shown in Figs. 8, 11 and 14), which can be identified by the fact that the magnitude of the secondary flow approach the maximum on the floor near the corner (as shown in Fig. 4). Under the restriction of the wall and the effect of the secondary flow, the distribution of particles near the wall looks unique.

Fig. 17 shows the ratio (p_c) of the number of particles in the corner to that in the whole duct, where particles are considered as their distance to the corner is less than 588. In Fig. 17, it is seen that the number of 10 μm, 50 μm and 100 μm particles in the corner remains stable within $t^+ < 20{,}000$, accounting for 2–4% of the total number of particles, where the ratio increases with particle size. However, the number of 500 μm particles located in the corner gradually decreases and finally approaches to the minimum level at 1%. This is because small and medium particles (10 μm, 50 μm and 100 μm) tend to be dominated by the drag force. As approaching the corner, particles tend to move away from it under the effect of the secondary flow. Such tendency increases with particle size decreasing due to its better flow ability with the flow. On the contrary, for the largest particle with 500 μm, its movement is dominated by gravity force. It likes to deposit the floor quickly under the effect of gravity. As particles with 500 μm deposit on the floor, the secondary flow push them leaving from the corner to the floor center (as shown in Figs. 8 and 14). As such, the ratio (p_c) of

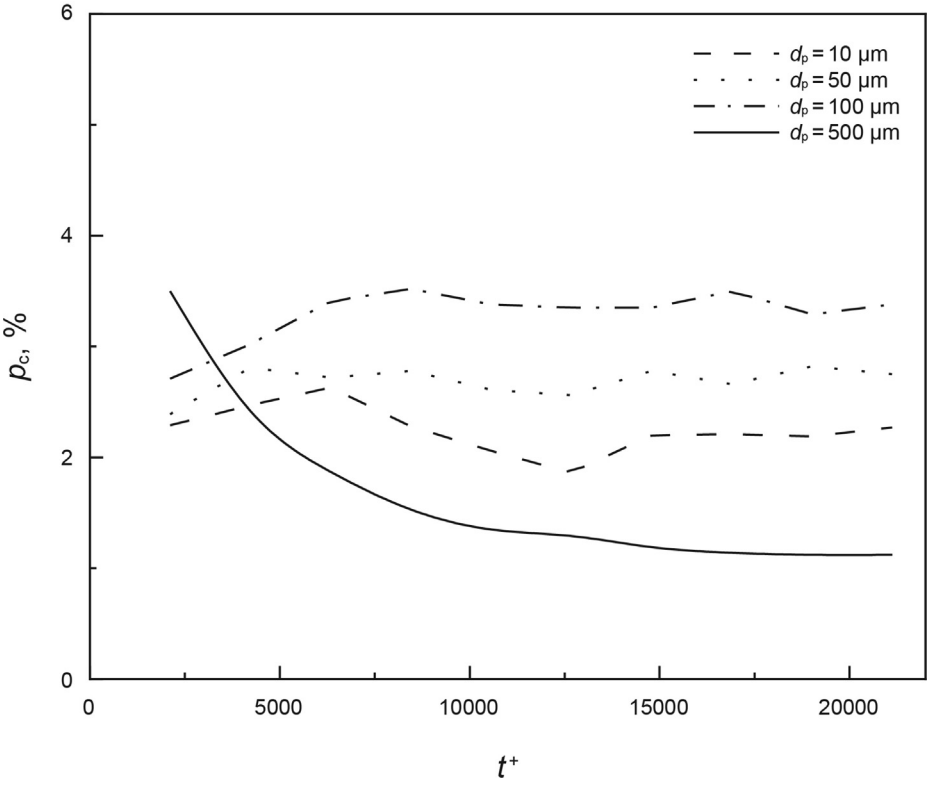

Fig. 17. Ratio of the particle number in corners to that in the whole duct, p_c.

500 μm is the minimum for all sized particles considered in this work.

To study particle dispersion in the duct flow quantitatively, the dispersion function in x - direction is introduced as following.

$$D^{+}_{x(t)} = \left(\sum_{i=1}^{N} \frac{\left(x^{+}_{i(t)} - x^{+}_{m(t)}\right)}{N} \right)^{\frac{1}{2}} \tag{13}$$

where N is the total number of particles in the computational domain at time t, $x^{+}_{i(t)}$ is the particle distribution in the spanwise direction x, and $x^{+}_{m(t)}$ is the mean value over the whole duct. The dispersion function in y direction is similar.

Fig. 18 shows particle dispersion at x- and y-directions with time. As shown in Fig. 18a, in the x direction, most mean position of particles fluctuates around 0 and its amplitude of fluctuation is less than 50. It is noted that the mean movement of the largest particle ($d_p = 500$ μm) at the spanwise direction (x-) fluctuates with higher frequency and lower amplitude. Fig. 18b shows the dispersion function at the x-direction for particles sized in the range of 10–500 μm It shows that such dispersion functions of small particles ($d_p = 10, 50, 100$ μm) remain stable with little difference. However, for the largest particle ($d_p = 500$ μm) the dispersion function at the x-direction decreases obviously with time indicating that they tend to concentrate together at x_m, which agrees well with the conclusion that the largest particles tend to gradually move towards the floor center (Fig. 14d). In Fig. 18c, particle dispersion foundation at the y-direction (the same as gravity direction) varies with particle size and time. For the smallest particles with 10 μm, the averaged position $y^{+}_{m} = 1175$ remains constant. For the medium particles (50 or 100 μm), they tend to deposit gradually under the effect of gravity. For the largest particles ($d_p = 500$ μm), they tend to deposit quickly at the floor. In Fig. 18d, for particles $d_p = 10, 50, 100$ μm, their y-dispersion functions are closed to each other. For the largest particle with $d_p = 500$ μm, at $t^{+} = 5000$ its mean position at y-direction (shown in Fig. 18c) is about zero but its dispersion function (shown in Fig. 18d) is still large at the same moment. It indicates that particles do not deposit all on the floor until $t^{+} = 10{,}000$ with $D^{+}_{y} \approx 0$.

The averaged values of slip velocity, drag force and lift force for particles sized $d_p = 10, 50, 100, 500$ μm at three moments

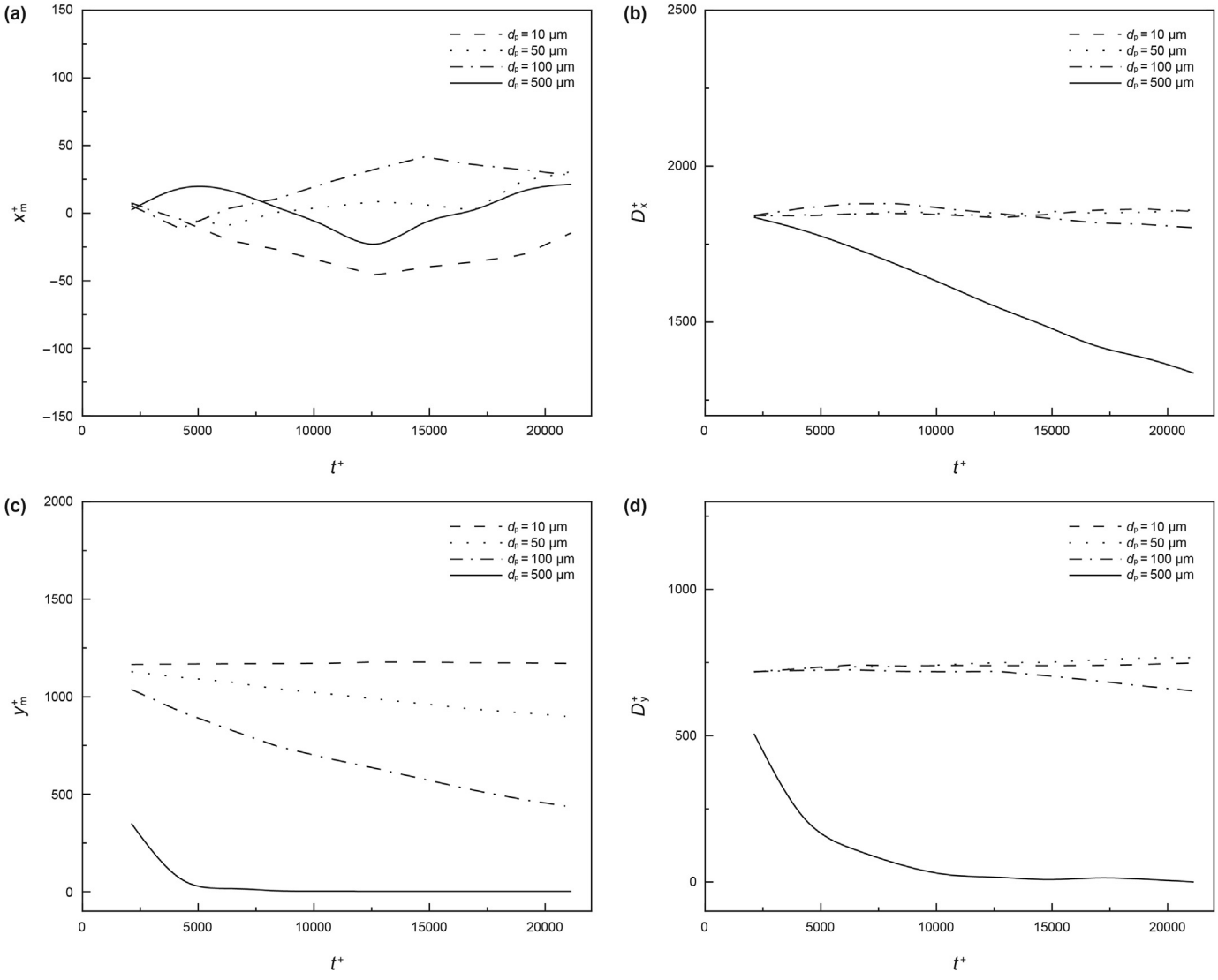

Fig. 18. Mean values (a)(c) and dispersion function (b)(d) of particle position with time.

Table 2
Average slip velocity and main forces.

$t+$	d_p, um	$\overline{u-u_p}^+(\times 10^{-3})$	$\overline{v-v_p}^+(\times 10^{-3})$	Drag force, $\times 10^{-13}$/N		Lift force, $\times 10^{-14}$/N	
				$\lvert\overline{F}_{Dx}\rvert$	$\lvert\overline{F}_{Dy}\rvert$	$\lvert\overline{F}_{Lx}\rvert$	$\lvert\overline{F}_{Ly}\rvert$
7042	10	4	3	40	91	6	6
	50	15	22	6010	9150	1560	1960
	100	24	52	22,100	47,600	8520	15,500
	500	39	13	247,000	152,000	299,000	49,500
14,085	10	4	3	40	90	6	6
	50	15	20	5580	8130	1420	1680
	100	20	39	17,900	35,400	7090	11,300
	500	49	4	304,000	27,100	39600	11,300
21,127	10	4	3	43	94	6	7
	50	14	19	5350	7950	1130	1660
	100	16	29	14,400	27,000	5900	8840
	500	41	4	251,000	24,600	327,000	10,400

($t^+ = 7042, 14{,}085, 21{,}127$) are listed in Table 2. Regarding the slip velocity, it is seen that, at the spanwise (x-) direction, it increases with particle size while at the vertical (y-) direction it is the same for particles $d_p = 10, 50, 100$ μm except for $d_p = 500$ μm. It is because at y-direction particle $d_p = 500$ μm deposit on the floor by gravity effect in a short time, where the velocity at y-direction is near zero but that at x-direction is still larger than other sized particles under the secondary flow effect.

In Table 2, it is seen that at the spanwise (x-) direction the drag force increases with particle size, which is independent of time. However, at the vertical (y-) direction the drag force increases with particle size at the initial stage ($t^+ = 7042$). At the moment $t^+ = 14{,}085, 21{,}127$, the drag force acting on largest particles ($d_p = 500$ μm) is lower that on $d_p = 100$ μm. On the other hand, forces acting on particles vary with particle size. For the smallest particle ($d_p = 10$ μm), the drag force is the largest, followed by the combined force of gravity and buoyancy (shown in Table 1), and the lift force is the smallest. In addition, drag force is at the same order of magnitude as gravity while lift force is smaller by two orders of magnitude than them. For particles $d_p = 50{,}100$ μm, the combined force of gravity and buoyancy is at the same order of magnitude as drag force. However, for the largest particle $d_p = 500$ μm, gravity is much larger than other forces. As such particles with 10, 50, 100 μm dominated by drag force are able to distribute throughout the duct, but particles with 500 μm is found to deposit on floor in a short time. It should be noted that the lift force acting on particles cannot be ignored. For particles with medium size ($d_p = 50{,}100{,}500$ μm), the lift force acting on them is smaller by one order of magnitude than drag force.

4. Conclusions

Similar to the square duct, the secondary flow can also be found in a turbulent semi-circular duct flow. The ceiling of the semi-circular duct is inward and two counter-rotating vortices formed in the corner are tangent at the diagonal, which causes the vortices near the ceiling wall occupy less space. For two walls, the ejection behavior induces at the end of two walls separately and interacts at the corner, which forms the secondary flow. The difference between the semi-circular duct and the square duct is that the secondary flow in a corner of the semi-circular duct is not symmetrical along the diagonal. Due to the effect of geometry, the secondary flow near ceiling is weaker than that near floor. The maximum of the secondary flow in the semi-circular duct is found to distribute near ceiling, floor, and diagonal lines. Although the characterizes of the secondary flow are different, the Reynolds stress generated in the semi-circular duct is under the same working mechanism as that in the square duct. In short, the secondary flows of semi-circular duct and square duct have the same generation mechanism.

Particle distribution in turbulent semi-circular duct flows depends on particle size. For example, 10 μm particles tend to distribute uniformly in the whole cross section while preferentially distribute near the top. For other particles 50, 100, 500 μm they tend to concentrate near the floor center as well as the corner. The largest particle (500 μm) deposit on the floor in a short time and move toward the floor center under the effect of the secondary flow so appear least at the corners. In addition, the effect of secondary flow is found to be more significant to dominate particle behavior than that of flow fluctuation. Based on force analysis, it is seen that most particles are dominated by drag force while for the largest particle (500 μm) gravity is much larger than other forces. Compared with the drag force, the lift force cannot be ignored particularly for particles 50 μm and 100 μm. In short, the behavior of smaller particles is dominated by the drag force (secondary flow) with their trajectories from the duct center toward corners, while that of larger particles is dominated by gravity because they tend to deposit to wall quickly and move toward the floor centre under the secondary flow effect.

In this work, due to electrostatic effect more particles are found to deposit near the floor and accumulate to become dense phase. For dense particle phase, particle-particle interaction become significant under electrostatic effect. Some particles may agglomerate becoming a big particle with non-spherical shape. Such big particle moves ahead and affects the fluid around it as indicated by Ren et al. (2019). On the other hand, such big particle affects the flow structure near wall boundary as indicated by Li et al. (2016). In this work, due to particle phase being dilute in most regions the effect of particles on flow and particle-particle interaction were ignored. Such assumption may not be suitable for particles as they agglomerate due to electrostatics, which will be overcome in the near future.

Acknowledgements

This work was supported by National Natural Science Foundation of China (No.51876221; 51776225) and High-end Foreign Expert Introduction Project (G20190001270; B18054). The authors would also like to express their gratitude to Profs W. P. Jones and M. Fairweather for providing the BOFFIN LES code and for many helpful discussions on its use.

References

Armenio, V., Fiorotto, V., 2001. The importance of the forces acting on particles in turbulent flows. Phys. Fluids 13, 2437–2440. https://doi.org/10.1063/1.1385390.

Biferale, L., Boffetta, G., Celani, A., Devenish, Be, Lanotte, A., Toschi, F., 2005. Lagrangian statistics of particle pairs in homogeneous isotropic turbulence. Phys. Fluids 17, 115101. https://doi.org/10.1063/1.2130742.

Bini, M., Jones, W.P., 2008. Large-eddy simulation of particle-laden turbulent flows. J. Fluid Mech. 614, 207–252. https://doi.org/10.1017/s0022112008003443.

Bradshaw, P., 1987. Turbulent secondary flows. Annu. Rev. Fluid Mech. 19, 53–74. https://doi.org/10.1146/annurev.fl.19.010187.000413.

Breuer, M., Rodi, W., 1994. Large-eddy simulation of turbulent flow through a straight square duct and a 180° bend. In: Voke, P.R., Kleiser, L., Chollet, J.P. (Eds.), Direct and Large-Eddy Simulation I. Fluid Mechanics and its Applications. Springer, Dordrecht.

Brundrett, E., Baines, W., 1964. The production and diffusion of vorticity in duct flow. J. Fluid Mech. 19, 375–394. https://doi.org/10.1017/S0022112064000799.

Burton, T.M., Eaton, J.K., 2005. Fully resolved simulations of particle-turbulence interaction. J. Fluid Mech. 545, 67–111. https://doi.org/10.1017/s0022112005006889.

Di Mare, L., Jones, W., 2003. LES of turbulent flow past a swept fence. Int. J. Heat Fluid Flow 24, 606–615. https://doi.org/10.1016/S0142-727X(03)00054-7.

Ferrante, A., Elghobashi, S., 2003. On the physical mechanisms of two-way coupling in particle-laden isotropic turbulence. Phys. Fluids 15, 315–329. https://doi.org/10.1063/1.1532731.

Friedlander, S., Johnstone, H., 1957. Deposition of suspended particles from turbulent gas strems. Ind. Eng. Chem. 49, 1151–1156. https://doi.org/10.1021/ie50571a039.

Gavrilakis, S., 1992. Numerical simulation of low-Reynolds-number turbulent flow through a straight square duct. J. Fluid Mech. 244, 101–129. https://doi.org/10.1017/S0022112092002982.

Germano, M., 1992. Turbulence - the filtering approach. J. Fluid Mech. 238, 325–336. https://doi.org/10.1017/S0022112092001733.

Germano, M., Piomelli, U., Moin, P., Cabot, W., 1991. A dynamic subgrid-scale eddy viscosity model. Phys. Fluids 3, 1760–1765. https://doi.org/10.1063/1.857955.

Gessner, F.B., Jones, J.B., 1965. On some aspects of fully-developed turbulent flow in rectangular channels. J. Fluid Mech. 23, 689–713. https://doi.org/10.1017/S0022112065001635.

Hadinoto, K., Curtis, J.S., 2009. Reynolds number dependence of gas-phase turbulence in particle-laden flows: effects of particle inertia and particle loading. Powder Technol. 195, 119–127. https://doi.org/10.1016/j.powtec.2009.05.022.

He, Z., Liu, Z.H., Chen, S., Weng, L., Zheng, C.G., 2005. Particle behavior in homogeneous isotropic turbulence. Acta Mech. Sin. 21, 112–120. https://doi.org/10.1007/s10409-005-0026-x.

Hurst, K.S., Rapley, C.W., 1991. Turbulent flow measurements in a 30/60 degree right triangular duct. Int. J. Heat Mass Tran. 34, 739–748. https://doi.org/10.1016/0017-9310(91)90121-T.

Huser, A., Biringen, S., 1993. Direct numerical simulation of turbulent flow in a square duct. J. Fluid Mech. 257, 65–95. https://doi.org/10.1017/S002211209300299X.

Js, S., 1963. General circulation experiments with the primitive equations. Mon. Weather Rev. 91, 99–164. https://doi.org/10.1175/1520-0493(1963)091.

Kajishima, T., 2004. Influence of particle rotation on the interaction between particle clusters and particle-induced turbulence. Int. J. Heat Fluid Flow 25, 721–728. https://doi.org/10.1016/j.ijheatfluidflow.2004.05.007.

Kussin, J., Sommerfeld, M., 2002. Experimental studies on particle behaviour and turbulence modification in horizontal channel flow with different wall roughness. Exp. Fluid 33, 143–159. https://doi.org/10.1007/s00348-002-0485-9.

Larsson, I.A.S., Lindmark, E.M., Lundström, T.S., Nathan, G.J., 2011. Secondary flow in semi-circular ducts. J. Fluid Eng. 133, 101206–101214. https://doi.org/10.1115/1.4004991.

Launder, B., Ying, W., 1972. Secondary flows in ducts of square cross-section. J. Fluid Mech. 54, 289–295. https://doi.org/10.1017/S0022112072000680.

Li, D., Luo, K., Fan, J.R., 2016. Modulation of turbulence by dispersed solid particles in a spatially developing flat-plate boundary layer. J. Fluid Mech. 802, 359–394. https://doi.org/10.1017/jfm.2016.406.

Li, D., Luo, K., Fan, J.R., 2017. Particle statistics in a two-way coupled turbulent boundary layer flow over a flat plate. Powder Technol. 305, 250–259. https://doi.org/10.1016/j.powtec.2016.09.063.

Liou, T.M., Chen, C.C., Chen, M.Y., 2003. Rotating effect on fluid flow in two smooth ducts connected by a 180-degree bend. J. Fluid Eng. 125, 138–148. https://doi.org/10.1115/1.1522413.

Madabhushi, R.K., Vanka, S.P., 1991. Large eddy simulation of turbulence-driven secondary flow in a square duct. Phys. Fluids 3, 2734–2745. https://doi.org/10.1063/1.858163.

Mallouppas, G., Wachem, B., 2013. Large Eddy Simulations of turbulent particle-laden channel flow. Int. J. Multiphas. Flow 54, 65–75.

Marin, O., Vinuesa, R., Obabko, A.V., Schlatter, P., 2016. Characterization of the secondary flow in hexagonal ducts. Phys. Fluids 28, 125101. https://doi.org/10.1063/1.4968844.

McCoy, D.D., Hanratty, T.J., 1977. Rate of deposition of droplets in annular two-phase flow. Int. J. Multiphas. Flow 3, 319–331. https://doi.org/10.1016/0301-9322(77)90012-X.

McLaughlin, J., 1989. Aerosol particle deposition in numerically simulated channel flow. Phys. Fluids 1, 1211–1224. https://doi.org/10.1063/1.857344.

Milojević, D., 1990. Lagrangian stochastic-deterministic (LSD) predictions of particle dispersion in turbulence. Part. Part. Syst. Char. 7, 181–190. https://doi.org/10.1002/ppsc.19900070132.

Nikuradse, J., 1930. Strömungswiderstand in rauhen rohren. J. Appl. Math. Mech. 1, 306–332.

Ogholaja, T., Njobuenwu, D.O., Fairweather, M., 2018. LES of particle collision and agglomeration in vertical channel flows. In: 28th European Symposium on Computer Aided Process Engineering, pp. 555–560.

Park, G.I., Bassenne, M., Urzay, J., Moin, P., 2017. A simple dynamic subgrid-scale model for LES of particle-laden turbulence. Phys Rev Fluids 2. https://doi.org/10.1103/PhysRevFluids.2.044301, 044301.

Pirozzoli, S., Modesti, D., Orlandi, P., Grasso, F., 2018. Turbulence and secondary motions in square duct flow. J. Fluid Mech. 840, 631–655. https://doi.org/10.1017/jfm.2018.66.

Porté-Agel, F., Meneveau, C., Parlange, M., 2000. A scale-dependent dynamic model for large-eddy simulation: application to a neutral atmospheric boundary layer. J. Fluid Mech. 415, 261–284. https://doi.org/10.1017/S0022112000008776.

Portela, L., Oliemans, R., 2003. Eulerian–Lagrangian DNS/LES of particle–turbulence interactions in wall-bounded flows. Int. J. Numer. Methods Fluid. 43, 1045–1065. https://doi.org/10.1002/fld.616.

Ren, A.X., Wang, T.Y., Tang, T.Q., He, Y.R., 2019. Non-spherical particle mixing behaviors by spherical inert particles assisted in a fluidized bed. Petrol. Sci. 17, 509–524. https://doi.org/10.1007/s12182-019-00401-4.

Rhie, C., Chow, W., 1983. Numerical study of the turbulent flow past an airfoil with trailing edge separation. AIAA J. 21, 1525–1532. https://doi.org/10.2514/3.8284.

Saffman, P., 1968. The lift on a small sphere in slow shear flow-corrigendum. J. Fluid Mech. 31 https://doi.org/10.1017/S0022112068999990, 624-624.

Salazar, J.P.L.C., De Jong, J., Cao, L.J., Woodward, S.H., Meng, H.U.I., Collins, L.R., 2008. Experimental and numerical investigation of inertial particle clustering in isotropic turbulence. J. Fluid Mech. 600, 245–256. https://doi.org/10.1017/s0022112008000372.

Sardina, G., Schlatter, P., Picano, F., Casciola, C.M., Brandt, L., Henningson, D.S., 2012. Self-similar transport of inertial particles in a turbulent boundary layer. J. Fluid Mech. 706, 584–596. https://doi.org/10.1088/1742-6596/318/5/052020.

Schneiders, L., Ma, Meinke, Schröder, W., 2017. Direct particle–fluid simulation of Kolmogorov-length-scale size particles in decaying isotropic turbulence. J. Fluid Mech. 819, 188–227. https://doi.org/10.1017/jfm.2017.171.

Shimizu, Y., Futaki, Y., Martin, C., 1992. Secondary flow and hydraulic losses within sinuous conduits of rectangular cross section. J. Fluid Eng. 114, 371–380. https://doi.org/10.1115/1.2910072.

Squires, K.D., Eaton, J.K., 1990. Particle response and turbulence modification in isotropic turbulence. Phys. Fluids 2, 1191–1203. https://doi.org/10.1063/1.857620.

Vidal, A., Vinuesa, R., Schlatter, P., Nagib, H.M., 2017. Influence of corner geometry on the secondary flow in turbulent square ducts. Int. J. Heat Fluid Flow 67, 69–78. https://doi.org/10.1016/j.ijheatfluidflow.2017.07.009.

Vinuesa, R., Noorani, A., Lozano-Durán, A., Khoury, G.K.E., Schlatter, P., Fischer, P.F., Nagib, H.M., 2014. Aspect ratio effects in turbulent duct flows studied through direct numerical simulation. J. Turbul. 15, 677–706. https://doi.org/10.1080/14685248.2014.925623.

Vinuesa, R., Prus, C., Schlatter, P., Nagib, H.M., 2016. Convergence of numerical simulations of turbulent wall-bounded flows and mean cross-flow structure of rectangular ducts. Meccanica 51, 3025–3042. https://doi.org/10.1007/s11012-016-0558-0.

Vreman, A.W., 2007. Turbulence characteristics of particle-laden pipe flow. J. Fluid Mech. 584, 235–279. https://doi.org/10.1017/s0022112007006556.

Wang, Q., Squires, K., Chen, M., McLaughlin, J., 1997. On the role of the lift force in turbulence simulations of particle deposition. Int. J. Multiphas. Flow 23, 749–763. https://doi.org/10.1016/S0301-9322(97)00014-1.

Westra, R., Broersma, L., Andel, K., Kruyt, N., 2010. PIV measurements and CFD computations of secondary flow in a centrifugal pump impeller. J. Fluid Eng. 132 https://doi.org/10.1115/1.4001803, 061104.

Winkler, C., Rani, S., Vanka, S.P., 2006. A numerical study of particle wall-deposition in a turbulent square duct flow. Powder Technol. 170, 12–25. https://doi.org/10.1016/j.powtec.2006.08.009.

Wood, N.B., 1981. A simple method for the calculation of turbulent deposition to smooth and rough surfaces. J. Aerosol Sci. 12, 275–290. https://doi.org/10.1016/0021-8502(81)90127-0.

Yao, J., Fairweather, M., 2010. Inertial particle resuspension in a turbulent, square duct flow. Phys. Fluids 22. https://doi.org/10.1063/1.3336013, 033303.

Yao, J., Fairweather, M., 2012. Particle deposition in turbulent duct flows. Chem. Eng. Sci. 84, 781–800. https://doi.org/10.1016/j.ces.2012.09.020.

Yao, J., Zhang, Y., Wang, C.H., Liang, Y., 2006. On the electrostatic equilibrium of granular flow in pneumatic conveying systems. AIChE J. 52, 3775–3793. https://doi.org/10.1002/aic.10991.

Yao, J., Zhang, Y., Wang, C.H., Matsusaka, S., Masuda, H., 2004. Electrostatics of the granular flow in a pneumatic conveying system. Ind. Eng. Chem. Res. 43, 7181–7199. https://doi.org/10.1021/ie049661l.

Young, J., Leeming, A., 1997. A theory of particle deposition in turbulent pipe flow. J. Fluid Mech. 340, 129–159. https://doi.org/10.1017/S0022112097005284.

Zhao, Y.L., Tang, C.Y., Yao, J., Zeng, Z.H., Dong, S.G., 2020. Investigation of erosion behavior of 304 stainless steel under solid–liquid jet flow impinging at 30°. Petrol. Sci. 17, 1135–1150. https://doi.org/10.1007/s12182-020-00473-7.